

Two-loop QCD corrections to ZH and off-shell Z boson pair production in gluon fusion

Joshua Davies^a, Dominik Grau^b, Kay Schönwald^c,
Matthias Steinhauser^b, Daniel Stremmer^b, Marco Vitti^{b,d}

(a) *Department of Mathematical Sciences, University of Liverpool, Liverpool, L69 3BX, UK*

(b) *Institut für Theoretische Teilchenphysik*

Karlsruhe Institute of Technology (KIT)

Wolfgang-Gaede Straße 1, 76131 Karlsruhe, Germany

(c) *Physik-Institut, Universität Zürich, Winterthurerstrasse 190,
8057 Zürich, Switzerland*

(d) *Institut für Astroteilchenphysik, Karlsruhe Institute of Technology (KIT),
Hermann-von-Helmholtz-Platz 1, 76344 Eggenstein-Leopoldshafen, Germany, Germany*

Abstract

We compute two-loop corrections to the associated production of a Higgs boson with a Z boson and to off-shell Z boson pair production in the gluon fusion channel, mediated by a heavy quark. We perform deep expansions in the high-energy region and around the forward limit and show that their combination covers the whole phase space. Our results constitute the next-to-leading order virtual corrections to these processes. Their numerical evaluation is fast and the dependence on all parameters is maintained, thus a change of parameter values or renormalization scheme is straightforward. As a by-product of our calculation, we also obtain the two-loop heavy quark mediated virtual corrections to the processes of off-shell di-photon and photon- Z production.

1 Introduction

The high-luminosity phase of the LHC will require accurate predictions for the gluon-initiated production of pairs of massive bosons, which we denote generically as $gg \rightarrow XY$. The next-to-leading-order (NLO) QCD corrections mediated by heavy-quark loops are hard to compute because of the many scales involved in this class of processes. This is particularly true for the box-type diagrams (see Fig. 1) which appear in the virtual corrections.

In this context the use of analytic expansions is known to be beneficial, allowing the results to be expressed in terms of simpler integrals which are relatively fast to evaluate numerically, while retaining the dependence on all the parameters involved. In this paper we are interested in one of the most complicated cases, in which the momenta of the two final-state particles are associated to different scales. The calculations involve five scales: the top quark mass m_t , the Mandelstam variables s and t , and the two (different) virtualities of the final-state bosons q_X^2 and q_Y^2 .

This class of processes includes $gg \rightarrow ZH$ and off-shell¹ $gg \rightarrow ZZ$, denoted as $gg \rightarrow Z^*Z^*$. The former is a non-negligible contribution to associated ZH production at the LHC, and represents one of the main sources of theoretical uncertainty in current measurements [1–4]. The top-mediated corrections to $gg \rightarrow ZZ$ are most important because of the interference between the Higgs-mediated and the non-resonant amplitudes, which has been used to put indirect constraints on the total decay width of the Higgs boson [5–7].

The LO contribution to $gg \rightarrow ZH$ and $gg \rightarrow ZZ$ is loop-induced and has been computed in Refs. [8–11]. At NLO in QCD, expansion results are available for the large-mass expansion (LME) [12–15], the high-energy expansion [13, 16], the small-mass expansion [17] and the p_T expansion [18, 19]. Numerical results have been presented in Refs. [20–23]. As a first result of this paper, we provide results for the t -expansion [24] of $gg \rightarrow ZH$ and top-quark mediated $gg \rightarrow Z^*Z^*$ including higher-order terms than Refs. [18, 19], and we provide new terms in the high-energy expansion. In the case of $gg \rightarrow ZZ$ we allow the Z bosons to be off-shell. This is an advantage of the analytic approach; the same methods can be applied in a straightforward way, although the intermediate and final expressions become larger. On the other hand, introducing an additional mass scale into the calculations of Refs. [21, 23] would lead to a significant increase in complexity. The helicity amplitudes for the light-quark mediated contribution to on-shell $gg \rightarrow ZZ$ can be found in Refs. [25, 26].

The possibility to rely only on analytic approximations for the virtual corrections of similar gg -initiated processes has been discussed in Refs. [24, 27], showing that the expansions in the forward limit and in the high-energy limit can be combined in such a way that the complete phase space is covered with an accuracy at the percent level. As a second result of

¹Note that in the literature *off-shell* often refers to the case in which the Higgs boson in the triangle-type diagrams of Fig. 1 is off-shell, as opposed to resonant single-Higgs production. Here, we are rather interested in the case in which the final-state Z bosons are off-shell.

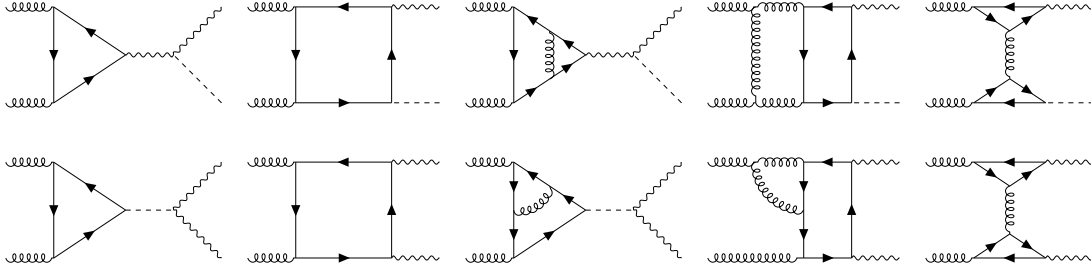


Figure 1: Sample Feynman diagrams contributing to $gg \rightarrow ZH$ (top) and $gg \rightarrow ZZ$ (bottom). Straight, wavy, curly and dashed lines refer to quarks, Z bosons, gluons and Higgs bosons, respectively.

this paper, we combine the new results for the two approximations following Ref. [24]. For $gg \rightarrow ZH$, the combination of the high-energy expansion [13] and the p_T expansion [18] has been presented in Ref. [28]. However, this analysis has the possible shortcoming that only three expansion terms for $p_T \rightarrow 0$ have been considered, and furthermore only 13 expansion terms in the high-energy limit have been included. In this work, we improve the description of $gg \rightarrow ZH$ in both regions of phase space: our expansion in the forward limit includes terms up to t^5 and $m_{Z,H}^8$, and we use a deep high-energy expansion which includes terms up to m_t^{112} and $m_{Z,H}^4$.

Our results for $gg \rightarrow Z^*Z^*$ can be used to obtain the helicity amplitudes for $gg \rightarrow \gamma^*\gamma^*$ and $gg \rightarrow Z^*\gamma^*$ by dropping the triangle contributions, setting the axial-vector coupling of the Z boson to zero, and replacing either both or one of the Zt couplings with the γt coupling. Numerical results for on-shell di-photon production can be found in Refs. [29,30] and recent exact calculations of the helicity amplitudes are available from [31,32].

The remainder of the paper is structured as follows: in the next section we provide technical details common to both processes and describe the procedure to obtain ultraviolet and infrared finite results. We then discuss off-shell Z boson pair production in Section 3 and $gg \rightarrow ZH$ in Section 4. At one-loop order we compare our approximations to the exact results. At two loops we show that the expansions in the forward limit and the high-energy limit agree for intermediate values of the transverse momentum p_T . For both processes we compare the total NLO virtual finite corrections to precise numerical results. We conclude in Section 5. In the Appendix we present results for the projectors to one of the helicity amplitudes for $gg \rightarrow Z^*Z^*$.

2 Technical details

2.1 Kinematics

We consider the scattering of two gluons in the initial state with momenta q_1 and q_2 into two massive particles in the final state, $gg \rightarrow XY$, with momenta q_3 and q_4 . The Mandelstam variables are then given by

$$s = (q_1 + q_2)^2, \quad t = (q_1 + q_3)^2, \quad u = (q_1 + q_4)^2, \quad (1)$$

where all momenta are incoming. Furthermore we have

$$q_1^2 = q_2^2 = 0. \quad (2)$$

For the production of on-shell particles we have

$$q_3^2 = q_X^2 = m_X^2, \quad q_4^2 = q_Y^2 = m_Y^2, \quad (3)$$

where in general m_X and m_Y are allowed to be different and the transverse momentum of the final-state particles is given by

$$p_T^2 = \frac{u t - q_3^2 q_4^2}{s}. \quad (4)$$

The (internal) top quark mass is denoted by m_t .

2.2 Amplitude construction

For the computation of the amplitudes in terms of scalar integrals we use a well-tested and automated setup. The diagrams required for the computation of the amplitudes for $gg \rightarrow ZH$ and $gg \rightarrow Z^*Z^*$ are generated with **qgraf** [33]. Afterwards, we use **tapir** [34] and **exp** [35,36] to map the diagrams onto integral families which are exact in all kinematic parameters. The output is converted to **FORM** [37] notation, which is used by the in-house “**calc**” setup to perform the Dirac and color algebra and finally provide the amplitudes expressed in terms of scalar Feynman integrals. The output is then further processed to obtain expansions in the high-energy and forward limits. We discuss the details of these expansions in the following sections.

2.3 Integral expansions

In this paper we perform two kinds of expansion: around the forward limit and for high energies. It has been shown for various $2 \rightarrow 2$ processes that the combination of these expansions leads to precise results over the whole phase space region [19,22,24,27,28,38]. We follow the approach of Ref. [24] and compute a Taylor expansion in the Mandelstam variable t . For the high-energy expansion we use the approach developed in Refs. [39,40].

We have two approaches to compute the t expansion (see below for more details):

- (i) expansion of the amplitude before reduction to master integrals,
- (ii) expansion of the master integrals after integration-by-parts (IBP) reduction.

We apply both approaches and use the agreement of the final results as a consistency check. In approach (i) we perform a simultaneous expansion in t and the final-state masses whereas in approach (ii) we first perform a Taylor expansion in the final-state masses and then apply an IBP reduction to obtain the amplitude in terms of t -dependent master integrals, which are subsequently expanded. We use **Kira** [41] and **FIRE** [42, 43] for the IBP reductions.

The high-energy expansion follows approach (ii) only, since approach (i) would lead to a complicated asymptotic expansion. Note that the amplitude in terms of master integrals, before expansion, is identical to that of the t expansion in approach (ii).

2.3.1 Forward expansion at the amplitude level

Our amplitudes have an analytic dependence on t , allowing us to perform a straightforward Taylor expansion of the integrands in the variable $\delta q = q_1 + q_3$. The expansion of the denominators produces numerator scalar products of the form $\delta q \cdot q_i$, where q_i is one of the external momenta. Here we use the kinematics given in Eqs. (1) to (3) in order to express them in terms of invariants.² This produces a simultaneous expansion³ in t , q_3^2 and q_4^2 .

The expansion in δq also leads to scalar products $\delta q \cdot p_i$, where p_i is a loop momentum. Here we perform a tensor reduction which eliminates q_3 from the numerator. We use the program **OPITeR** [45] in order to generate **FORM** [37] code which we can include in our setup. Since the expansion in δq eliminates q_3 from the denominators of the integrands, the resulting integrals depend only on s/m_t^2 and not on t , q_3^2 nor q_4^2 .

We manage to compute expansion terms up to $t^{n_t}(q_3^2)^{n_3}(q_4^2)^{n_4}$ with $n_t + n_3 + n_4 \leq 4$ for both processes. This leads to tensor integrals up to rank 14, which constitutes one of the main bottlenecks of this approach. In this expansion of the helicity amplitude \mathcal{A}_{++00} of $gg \rightarrow Z^*Z^*$ (see Section 3) we encounter tensor integrals only up to rank 10, which allows us to extend the expansion to also include the terms $n_t + n_3 + n_4 = 5$ in this particular case.

²The use of the “full” kinematics with massive final-state particles is different from the approach suggested in Ref. [24]. There an expansion in q_3^2 and q_4^2 is performed first, followed by a δq expansion in massless kinematics (where $q_3^2 = q_4^2 = 0$).

Expanding the scalar integrals first in the final-state masses generates spurious negative powers of t , which only cancel after the expansion in δq . Thus, as compared to the approach used in this paper, a deeper expansion in δq is necessary to arrive at the desired order in t in the final expression.

³A similar approach has been introduced in Ref. [44].

2.3.2 Forward expansion of the master integrals

In the second approach to obtain the t expansion we do not expand the integrand but first perform a reduction to master integrals and then expand them. To simplify the reduction problem we expand each scalar integral in the final-state masses q_3^2 and q_4^2 using the program `LiteRed` [46]. This leads to a reduction problem which only depends on s , t and m_t^2 . It has already been studied in Refs. [39,40], where 161 two-loop master integrals were identified. The t expansion of these master integrals was constructed in Ref. [24] with the help of the semi-analytic “expand and match” approach [47–49].

The bottleneck in this approach are the huge intermediate expressions which are generated after the expansion in q_3^2 and q_4^2 and the insertion of the IBP reduction tables. Once the t expansions of the master integrals are inserted, much more compact expressions are obtained. We manage to compute quartic terms in q_3 and q_4 and an expansion up to t^5 for $gg \rightarrow ZH$ and t^{10} for $gg \rightarrow Z^*Z^*$. In all expansion terms which overlap with those obtained in Section 2.3.1 we find agreement.

Our final results for the helicity amplitudes use a combination of both t -expansion approaches. The contributions have the form $t^{n_t}(q_3^2)^{n_3}(q_4^2)^{n_4}$. For $n_3+n_4 = 0, 1, 2$ we include all terms up to $n_t \leq 5$ (ZH) and $n_t \leq 10$ (Z^*Z^*), using approach (ii). “Above” these we additionally include terms with $n_t + n_3 + n_4 \leq 4$, computed using approach (i).⁴

2.3.3 High-energy expansion of master integrals

The starting point for the high-energy expansion is the same amplitude in terms of the 161 two-loop master integrals as for the t expansion. Thus, the agreement of the t expansions obtained in Sections 2.3.1 and 2.3.2 imposes a strong check on our high-energy results. After expanding the coefficients for $m_t \rightarrow 0$ and inserting the high-energy expansion of the master integrals from Refs. [24, 39, 40, 50] we obtain results for the form factors and helicity amplitudes expanded up to $(q_3^2)^{n_3}(q_4^2)^{n_4}$ with $n_3 + n_4 \leq 2$ and up to m_t^{112} .

We use these deep expansions to construct Padé approximants in the variable m_t . This is achieved by first inserting numerical values for all kinematic variables and for the $\log(m_t)$ terms, which leads to a polynomial in m_t with the highest exponent N . Afterwards we compute a set of Padé approximants where N is varied in a given range. Their combination provides, for each phase-space point, a central value and an uncertainty estimate. For more details we refer to Ref. [16]. Note that it is important to include expansion terms up to about m_t^{80} ; including more terms only leads to a marginal change of the numerical results. For practical reasons we include for $gg \rightarrow Z^*Z^*$ terms up to m_t^{100} and for $gg \rightarrow ZH$ terms up to m_t^{112} .

⁴For the helicity amplitude \mathcal{A}_{++00} of $gg \rightarrow Z^*Z^*$ we include terms to $n_t + n_3 + n_4 \leq 5$, as discussed in Section 2.3.2.

2.4 Ultraviolet renormalization and infrared subtraction

To treat the ultraviolet divergences we work in the six-flavour theory and renormalize the top quark mass and the gluon wave function on shell and the strong coupling α_s in the $\overline{\text{MS}}$ scheme. For the process $gg \rightarrow ZH$ we have additional (finite) renormalization constants due to our treatment of γ_5 . They are different for axial-vector (“A”) currents, and pseudo-scalar (“P”) currents which appear due to s -channel Goldstone bosons in the triangle diagrams, and are given by [51]:

$$\begin{aligned} Z_{5A} &= 1 - \frac{\alpha_s}{\pi} C_F + \mathcal{O}(\epsilon), \\ Z_{5P} &= 1 - 2 \frac{\alpha_s}{\pi} C_F + \mathcal{O}(\epsilon), \end{aligned}$$

with $C_F = 4/3$. At this point all remaining poles in ϵ are of infrared nature. Since they are usually treated in the five-flavour theory we switch from $\alpha_s^{(6)}$ to $\alpha_s^{(5)}$.

For the subtraction of the infrared poles we follow Ref. [52] and compute⁵

$$F^{(1)} = F^{(1),\text{IR}} - K_g^{(1)} F^{(0)}. \quad (5)$$

Here the superscripts “(0)” and “(1)” indicate the LO and NLO contributions to the form factors. $F^{(1),\text{IR}}$ is ultraviolet renormalized but still infrared divergent and $F^{(1)}$ on the left-hand side is finite. In our conventions $K_g^{(1)}$ is given by

$$K_g^{(1)} = - \left(\frac{\mu^2}{-s - i\delta} \right)^\epsilon \frac{e^{\epsilon\gamma_E}}{2\Gamma(1-\epsilon)} \left[\frac{C_A}{\epsilon^2} + \frac{1}{\epsilon} \left(\frac{11}{6} C_A - \frac{1}{3} n_f \right) \right], \quad (6)$$

where $C_A = 3$, $n_f = 5$ and γ_E is Euler’s constant.

3 $gg \rightarrow Z^* Z^*$

3.1 Amplitudes and projectors

The amplitude for $gg \rightarrow Z^* Z^*$ can be written as

$$\mathcal{A}_{\lambda_1 \lambda_2 \lambda_3 \lambda_4}(q_1, q_2, q_3, q_4) = \mathcal{A}_{\mu\nu\rho\sigma}(q_1, q_2, q_3, q_4) \epsilon_{\lambda_1}^\mu(q_1) \epsilon_{\lambda_2}^\nu(q_2) \epsilon_{\lambda_3}^{*\rho}(q_3) \epsilon_{\lambda_4}^{*\sigma}(q_4), \quad (7)$$

where the polarization indices take the values $\{+, -\}$ for the gluons and $\{+, -, 0\}$ for the Z bosons. The most general form consists of 138 parity-even tensor structures, but this number can be reduced to 20, see Refs. [16, 25, 26], by taking into account the transversality of the external particles ($\varepsilon(q_i) \cdot q_i = 0$) and by fixing the gauge of the gluon polarization vectors. We consider an axial gauge with the reference momentum q_2 for $\varepsilon(q_1)$ and q_1 for

⁵We present the formula for form factors; the application to helicity amplitudes is in complete analogy.

$\varepsilon(q_2)$, so that the two gauge conditions are given by $\varepsilon(q_1) \cdot q_2 = 0$ and $\varepsilon(q_2) \cdot q_1 = 0$. The polarization sums are given by

$$\sum_{\lambda} \varepsilon_{\lambda}^{\mu}(q_1) \varepsilon_{\lambda}^{*\nu}(q_1) = \sum_{\lambda} \varepsilon_{\lambda}^{\mu}(q_2) \varepsilon_{\lambda}^{*\nu}(q_2) = -g^{\mu\nu} + \frac{q_1^{\mu} q_2^{\nu} + q_2^{\mu} q_1^{\nu}}{q_1 \cdot q_2}. \quad (8)$$

On the other hand, the polarization sums of the two Z bosons lead to

$$\sum_{\lambda} \varepsilon_{\lambda}^{\mu}(q_i) \varepsilon_{\lambda}^{*\nu}(q_i) = -g^{\mu\nu} + \frac{q_i^{\mu} q_i^{\nu}}{q_i^2} \quad (9)$$

for $i = 3, 4$. We write the amplitude as

$$\mathcal{A}^{\mu\nu\rho\sigma}(q_1, q_2, q_3, q_4) = \sum_{i=1}^{20} F_i(s, t, q_3^2, q_4^2) T_i^{\mu\nu\rho\sigma}, \quad (10)$$

where the 20 tensor structures are given by

$$\begin{aligned} T_1^{\mu\nu\rho\sigma} &= s^2 g^{\mu\nu} g^{\rho\sigma}, & T_2^{\mu\nu\rho\sigma} &= s^2 g^{\mu\rho} g^{\nu\sigma}, & T_3^{\mu\nu\rho\sigma} &= s^2 g^{\mu\sigma} g^{\nu\rho}, & T_4^{\mu\nu\rho\sigma} &= s g^{\mu\nu} q_1^{\rho} q_1^{\sigma}, \\ T_5^{\mu\nu\rho\sigma} &= s g^{\mu\nu} q_1^{\rho} q_2^{\sigma}, & T_6^{\mu\nu\rho\sigma} &= s g^{\mu\nu} q_1^{\rho} q_2^{\rho}, & T_7^{\mu\nu\rho\sigma} &= s g^{\mu\nu} q_2^{\rho} q_2^{\sigma}, & T_8^{\mu\nu\rho\sigma} &= s g^{\mu\rho} q_1^{\sigma} q_3^{\nu}, \\ T_9^{\mu\nu\rho\sigma} &= s g^{\mu\rho} q_2^{\sigma} q_3^{\nu}, & T_{10}^{\mu\nu\rho\sigma} &= s g^{\mu\sigma} q_1^{\rho} q_3^{\nu}, & T_{11}^{\mu\nu\rho\sigma} &= s g^{\mu\sigma} q_2^{\rho} q_3^{\nu}, & T_{12}^{\mu\nu\rho\sigma} &= s g^{\nu\rho} q_1^{\sigma} q_3^{\mu}, \\ T_{13}^{\mu\nu\rho\sigma} &= s g^{\nu\rho} q_2^{\sigma} q_3^{\mu}, & T_{14}^{\mu\nu\rho\sigma} &= s g^{\nu\sigma} q_1^{\rho} q_3^{\mu}, & T_{15}^{\mu\nu\rho\sigma} &= s g^{\nu\sigma} q_2^{\rho} q_3^{\mu}, & T_{16}^{\mu\nu\rho\sigma} &= s g^{\rho\sigma} q_3^{\mu} q_3^{\nu}, \\ T_{17}^{\mu\nu\rho\sigma} &= q_1^{\rho} q_1^{\sigma} q_3^{\mu} q_3^{\nu}, & T_{18}^{\mu\nu\rho\sigma} &= q_1^{\rho} q_2^{\sigma} q_3^{\mu} q_3^{\nu}, & T_{19}^{\mu\nu\rho\sigma} &= q_1^{\sigma} q_2^{\rho} q_3^{\mu} q_3^{\nu}, & T_{20}^{\mu\nu\rho\sigma} &= q_2^{\rho} q_2^{\sigma} q_3^{\mu} q_3^{\nu}. \end{aligned} \quad (11)$$

The ordering of the tensor structure is the same as in Ref. [21] but with additional factors of s such that all tensor structures have the same mass dimension. Note that the amplitude $\mathcal{A}^{\mu\nu\rho\sigma}$ is dimensionless and that the form factors have mass dimension -4 .

We introduce the projectors $P_i^{\mu\nu\rho\sigma}$ for the form factors F_i via the ansatz

$$P_i^{\mu\nu\rho\sigma} = \sum_{j=1}^{20} c_{ij} T_j^{\mu\nu\rho\sigma}, \quad (12)$$

and determine the coefficients $c_{ij}(s, t, q_3^2, q_4^2)$ by requiring

$$F_i = P_i^{\mu\nu\rho\sigma} \sum_{\lambda_1, \lambda_2, \lambda_3, \lambda_4} \varepsilon_{1,\mu}^* \varepsilon_{1,\mu'} \varepsilon_{2,\nu}^* \varepsilon_{2,\nu'} \varepsilon_{3,\rho}^* \varepsilon_{3,\rho'} \varepsilon_{4,\sigma}^* \varepsilon_{4,\sigma'} \mathcal{A}^{\mu'\nu'\rho'\sigma'}, \quad (13)$$

with $\varepsilon_{i,\mu}^{(*)} \equiv \varepsilon_{\lambda_i,\mu}^{(*)}(q_i)$. The summation over the polarizations as introduced in Eq. (13) guarantees that only the 20 tensor structures from Eq. (11), and not all possible 138 tensor structures, have to be considered.

In our practical calculation we first compute the projectors $P_i^{\mu\nu\rho\sigma}$ and use them to construct the projectors for the helicity amplitudes $\mathcal{A}_{\lambda_1 \lambda_2 \lambda_3 \lambda_4}$ which are given by

$$\mathcal{A}_{\lambda_1 \lambda_2 \lambda_3 \lambda_4} = \mathcal{P}_{\lambda_1 \lambda_2 \lambda_3 \lambda_4}^{\mu\nu\rho\sigma} \sum_{\lambda'_1, \lambda'_2, \lambda'_3, \lambda'_4} \varepsilon_{1,\mu}^* \varepsilon_{1,\mu'} \varepsilon_{2,\nu}^* \varepsilon_{2,\nu'} \varepsilon_{3,\rho}^* \varepsilon_{3,\rho'} \varepsilon_{4,\sigma}^* \varepsilon_{4,\sigma'} \mathcal{A}^{\mu'\nu'\rho'\sigma'}. \quad (14)$$

The projectors $\mathcal{P}_{\lambda_1\lambda_2\lambda_3\lambda_4}^{\mu\nu\rho\sigma}$ are obtained from the multiplication of the 20 projectors $P_i^{\mu\nu\rho\sigma}$ by the contraction of the tensor structures $T_i^{\mu\nu\rho\sigma}$ with the polarization vectors of the gluons and Z bosons as

$$\mathcal{P}_{\lambda_1\lambda_2\lambda_3\lambda_4}^{\mu\nu\rho\sigma} = \sum_{i=1}^{20} P_i^{\mu\nu\rho\sigma} \left(\epsilon_{\lambda_1}^{\mu'}(q_1) \epsilon_{\lambda_2}^{\nu'}(q_2) \epsilon_{\lambda_3}^{*\rho'}(q_3) \epsilon_{\lambda_4}^{*\sigma'}(q_4) T_{i,\mu'\nu'\rho'\sigma'} \right) = \sum_{i=1}^{20} a_{\lambda_1\lambda_2\lambda_3\lambda_4}^{(i)} T_i^{\mu\nu\rho\sigma}. \quad (15)$$

The projectors for the helicity amplitudes are written as linear combinations of the 20 tensor structures $T_i^{\mu\nu\rho\sigma}$ and coefficients $a_{\lambda_1\lambda_2\lambda_3\lambda_4}^{(i)}(s, t, q_3^2, q_4^2)$, see right-hand side of Eq. (15). Explicit results for the $a_{\lambda_1\lambda_2\lambda_3\lambda_4}^{(i)}$ are obtained after specifying the polarization vectors as given below. For illustration, we provide explicit results for \mathcal{A}_{++00} in Appendix A; results for all helicity amplitudes can be found in the supplementary material of this paper [53].

We choose the same polarization vectors as in Ref. [21], extended to the case of two off-shell Z bosons, where we parametrize the four momenta as

$$\begin{aligned} q_1 &= \frac{\sqrt{s}}{2} \begin{pmatrix} 1 \\ 0 \\ 0 \\ 1 \end{pmatrix}, & q_3 &= \frac{\sqrt{s}}{2} \begin{pmatrix} -\left(1 + \frac{q_3^2}{s} - \frac{q_4^2}{s}\right) \\ -\beta \sin \theta \\ 0 \\ -\beta \cos \theta \end{pmatrix}, \\ q_2 &= \frac{\sqrt{s}}{2} \begin{pmatrix} 1 \\ 0 \\ 0 \\ -1 \end{pmatrix}, & q_4 &= \frac{\sqrt{s}}{2} \begin{pmatrix} -\left(1 - \frac{q_3^2}{s} + \frac{q_4^2}{s}\right) \\ \beta \sin \theta \\ 0 \\ \beta \cos \theta \end{pmatrix}, \end{aligned} \quad (16)$$

with

$$\beta = \sqrt{1 - 2 \frac{q_3^2 + q_4^2}{s} + \frac{(q_3^2 - q_4^2)^2}{s^2}}, \quad (17)$$

and the polarization vectors are given by

$$\begin{aligned} \varepsilon_{\pm}(q_1) = \varepsilon_{\mp}(q_2) &= \frac{1}{\sqrt{2}} \begin{pmatrix} 0 \\ \mp 1 \\ -i \\ 0 \end{pmatrix}, & \varepsilon_0(q_3) &= \frac{\sqrt{s}}{2\sqrt{q_3^2}} \begin{pmatrix} \beta \\ \sin \theta \left(1 + \frac{q_3^2}{s} - \frac{q_4^2}{s}\right) \\ 0 \\ \cos \theta \left(1 + \frac{q_3^2}{s} - \frac{q_4^2}{s}\right) \end{pmatrix}, \\ \varepsilon_{\pm}(q_3) = \varepsilon_{\mp}(q_4) &= \frac{1}{\sqrt{2}} \begin{pmatrix} 0 \\ \mp \cos \theta \\ -i \\ \pm \sin \theta \end{pmatrix}, & \varepsilon_0(q_4) &= \varepsilon_0(q_3) \Big|_{\theta \rightarrow \theta + \pi, q_3^2 \leftrightarrow q_4^2}. \end{aligned} \quad (18)$$

In practice we write the coefficients $a_{\lambda_1\lambda_2\lambda_3\lambda_4}^{(i)}$ in Eq. (15) as

$$a_{\lambda_1\lambda_2\lambda_3\lambda_4}^{(i)} = \frac{p_T^{b_{\lambda_1\lambda_2\lambda_3\lambda_4}}}{\beta^2 \sqrt{q_3^2}^{\delta_{\lambda_3 0}} \sqrt{q_4^2}^{\delta_{\lambda_4 0}}} \left(a_{\lambda_1\lambda_2\lambda_3\lambda_4}^{(i,\beta^0)} + \beta a_{\lambda_1\lambda_2\lambda_3\lambda_4}^{(i,\beta^1)} \right), \quad (19)$$

where $b_{\lambda_1\lambda_2\lambda_3\lambda_4}$ is either 0, 1 or 2, depending on the helicity amplitude. The coefficients are written in such a way that the normalization factor and the factor β in the brackets in Eq. (19) are hidden during the forward and high-energy expansions so that the helicity amplitudes are given in both cases by

$$\mathcal{A}_{\lambda_1\lambda_2\lambda_3\lambda_4} = \frac{p_T^{b_{\lambda_1\lambda_2\lambda_3\lambda_4}}}{\beta^2 \sqrt{q_3^2}^{\delta_{\lambda_3 0}} \sqrt{q_4^2}^{\delta_{\lambda_4 0}}} \left(\mathcal{A}_{\lambda_1\lambda_2\lambda_3\lambda_4}^{(\beta^0)} + \beta \mathcal{A}_{\lambda_1\lambda_2\lambda_3\lambda_4}^{(\beta^1)} \right), \quad (20)$$

where the latter term is zero for the helicity amplitudes $\mathcal{A}_{\lambda_1\lambda_2 00}$. The choice of the normalization factors ensures that the first expansion term of the forward expansion of $\mathcal{A}_{\lambda_1\lambda_2\lambda_3\lambda_4}^{(\beta^0)}$ and $\mathcal{A}_{\lambda_1\lambda_2\lambda_3\lambda_4}^{(\beta^1)}$ is independent of t , q_3^2 and q_4^2 . In addition, we have found that not expanding the factors of β drastically improves the convergence of the expansion in q_3^2 and q_4^2 , especially for small values of \sqrt{s} .

Due to several symmetries between the helicity amplitudes, see also Ref. [21], we find that just eight are independent which we choose as

$$\mathcal{A}_{++++}, \mathcal{A}_{++++-}, \mathcal{A}_{++-0}, \mathcal{A}_{++00}, \mathcal{A}_{+---}, \mathcal{A}_{+--+}, \mathcal{A}_{+-0}, \mathcal{A}_{+-00}. \quad (21)$$

All helicity amplitudes with $\lambda_1 = -$ can be obtained from those with $\lambda_1 = +$ with the relation

$$\mathcal{A}_{\lambda_1\lambda_2\lambda_3\lambda_4} = (-1)^{\delta_{\lambda_3 0} + \lambda_4 0} \mathcal{A}_{-\lambda_1 - \lambda_2 - \lambda_3 - \lambda_4}. \quad (22)$$

In addition, we use the following relations for the replacement $q_3^2 \leftrightarrow q_4^2$

$$\mathcal{A}_{++0-} = \mathcal{A}_{++-0} \Big|_{q_3^2 \leftrightarrow q_4^2}, \quad \mathcal{A}_{+-0-} = -\mathcal{A}_{+-+0} \Big|_{q_3^2 \leftrightarrow q_4^2}, \quad (23)$$

and the replacement $\beta \rightarrow -\beta$ provides relations

$$\begin{aligned} \mathcal{A}_{++--} &= \mathcal{A}_{++++} \Big|_{\beta \rightarrow -\beta}, & \mathcal{A}_{++-+} &= \mathcal{A}_{++++-} \Big|_{\beta \rightarrow -\beta}, \\ \mathcal{A}_{+--+} &= \mathcal{A}_{+---} \Big|_{\beta \rightarrow -\beta}, & \mathcal{A}_{+---} &= \mathcal{A}_{+--+} \Big|_{\beta \rightarrow -\beta}, \\ \mathcal{A}_{+++0} &= -\mathcal{A}_{++-0} \Big|_{\beta \rightarrow -\beta}, & \mathcal{A}_{++0+} &= -\mathcal{A}_{++-0} \Big|_{\beta \rightarrow -\beta}, \\ \mathcal{A}_{+-+0} &= -\mathcal{A}_{+-0} \Big|_{\beta \rightarrow -\beta}, & \mathcal{A}_{+-0+} &= -\mathcal{A}_{+-0} \Big|_{\beta \rightarrow -\beta}, \end{aligned} \quad (24)$$

to obtain the remaining helicity amplitudes. As an additional cross-check we have also calculated the helicity amplitudes \mathcal{A}_{++0-} and \mathcal{A}_{+-0-} , so that all remaining helicity amplitudes could in principle be obtained from only the relations coming from $\beta \rightarrow -\beta$. As another cross-check we have verified the following relations up to quadratic order in q_3 and q_4 in our results

$$\begin{aligned} \mathcal{A}_{++++} &= \mathcal{A}_{++++} \Big|_{q_3^2 \leftrightarrow q_4^2}, & \mathcal{A}_{+--+} &= \mathcal{A}_{+--+} \Big|_{q_3^2 \leftrightarrow q_4^2}, \\ \mathcal{A}_{++00} &= \mathcal{A}_{++00} \Big|_{q_3^2 \leftrightarrow q_4^2}, & \mathcal{A}_{+-00} &= \mathcal{A}_{+-00} \Big|_{q_3^2 \leftrightarrow q_4^2}, \\ \mathcal{A}_{++++-} &= \mathcal{A}_{++++-} \Big|_{q_3^2 \leftrightarrow q_4^2, \beta \rightarrow -\beta}, & \mathcal{A}_{+--+} &= \mathcal{A}_{+--+} \Big|_{q_3^2 \leftrightarrow q_4^2, \beta \rightarrow -\beta}, \end{aligned} \quad (25)$$

We define the perturbative expansion of the helicity amplitudes as

$$\mathcal{A}_{\lambda_1\lambda_2\lambda_3\lambda_4} = \frac{\alpha_s}{2\pi} \mathcal{A}_{\lambda_1\lambda_2\lambda_3\lambda_4}^{(0)} + \left(\frac{\alpha_s}{2\pi}\right)^2 \mathcal{A}_{\lambda_1\lambda_2\lambda_3\lambda_4}^{(1)} \quad (26)$$

and decompose them at each loop order according to the vector, axial-vector, triangle and double-triangle contribution

$$\mathcal{A}_{\lambda_1\lambda_2\lambda_3\lambda_4}^{(i)} = v_t^2 \mathcal{A}_{\lambda_1\lambda_2\lambda_3\lambda_4}^{(i),v_t^2} + a_t^2 \mathcal{A}_{\lambda_1\lambda_2\lambda_3\lambda_4}^{(i),a_t^2} + \frac{e^2}{s_w c_w} \frac{s}{s - m_h^2} \mathcal{A}_{\lambda_1\lambda_2\lambda_3\lambda_4}^{(i),\text{tri}} + \mathcal{A}_{\lambda_1\lambda_2\lambda_3\lambda_4}^{(i),\text{dt}}, \quad (27)$$

where v_t and a_t are given by

$$v_t = \frac{e}{2s_w c_w} (I_t^3 - 2Q_t s_w^2), \quad a_t = \frac{e}{2s_w c_w} I_t^3, \quad (28)$$

with $e = \sqrt{4\pi\alpha}$ where α is the fine structure constant, $Q_t = 2/3$ is the (fractional) electric charge of the top quark, $I_t^3 = 1/2$ is the third component of the weak isospin, and $s_w^2 = 1 - c_w^2$ with $c_w = \cos(\theta_W)$ being the cosine of the weak mixing angle. For the numerical results shown below we use $c_w = m_W/m_Z$ and $\sqrt{2}G_F = \pi\alpha/(m_W^2 s_w^2)$ and use the Fermi constant G_F and the W and Z boson masses as input.

In Sections 3.2, 3.3 and 3.4 we only discuss the results for the box contributions $\mathcal{A}_{\lambda_1\lambda_2\lambda_3\lambda_4}^{(i),v_t^2}$ and $\mathcal{A}_{\lambda_1\lambda_2\lambda_3\lambda_4}^{(i),a_t^2}$. We have checked that our high-energy expansions converge very quickly for the triangle contribution $\mathcal{A}_{\lambda_1\lambda_2\lambda_3\lambda_4}^{(i),\text{tri}}$. Analytic results for the double-triangle contribution can be found in Ref. [15] for on-shell Z bosons. To our knowledge, the off-shell result is not yet known. Note that the leading term of the t expansion corresponds to the exact result for the triangle form factors and helicity amplitudes.

In Ref. [16] the high-energy expansion of the form factors has been computed including terms up to m_t^{32} ; in this work we compute the eight helicity amplitudes in Eq. (21) including one hundred expansion terms in m_t .

3.2 One-loop results to $gg \rightarrow Z^* Z^*$

In this section we consider the one-loop helicity amplitudes and compare our approximations to the exact results. The exact one-loop results have been calculated with the `calc` setup without applying any expansions and are expressed in terms of scalar one-loop functions. We use `OneLOop` [54] for their numerical evaluation. We use the same number of expansion terms at one and two loops. For the high-energy expansion we have mass corrections up to $q_{3,4}^{\{0,2,4\}}$ and m_t terms up to 100. In addition, we construct a Padé approximation following Ref. [16], where we use expansions in m_t between m_t^{88} and m_t^{100} . For the $t \rightarrow 0$ expansion we consider mass corrections up to $q_{3,4}^{\{0,2,4\}}$ and terms up to t^{10} . In addition, we also include higher mass corrections up to $q_{3,4}^8$ with fewer expansion terms in t , that are obtained from the forward expansion at the amplitude level (“approach (i)”); this includes terms of the form $t^{n_t}(q_3^2)^{n_3}(q_4^2)^{n_4}$ with $n_t + n_3 + n_4 \leq 4$.

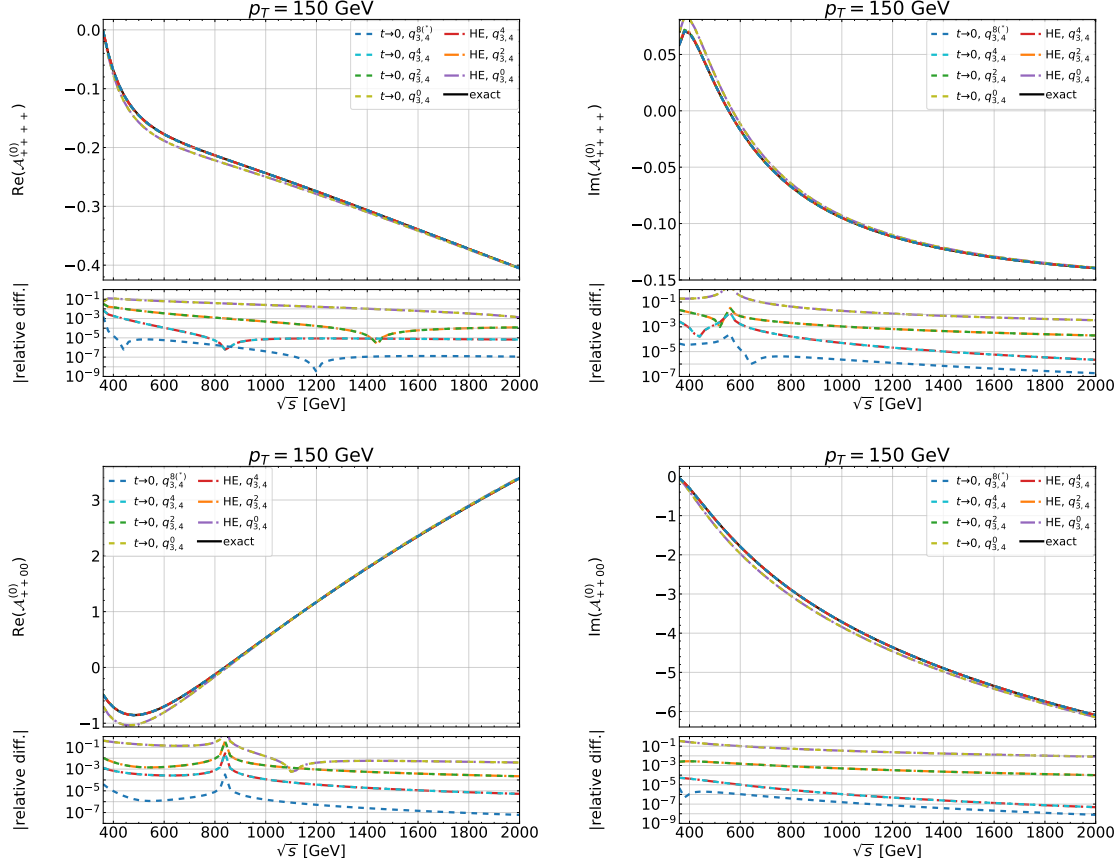


Figure 2: Real and imaginary parts of $\mathcal{A}_{++++}^{(0)}$ and $\mathcal{A}_{++00}^{(0)}$ as a function of \sqrt{s} for $p_T = 150$ GeV and $q_3^2 = q_4^2 = m_Z^2$. High-energy and $t \rightarrow 0$ expansions are shown, including mass corrections up to $q_{3,4}^{\{0,2,4\}}$. Also shown are higher mass corrections up to $q_{3,4}^8$ for the $t \rightarrow 0$ expansion with fewer expansion terms in t according to $t^{n_t}(q_3^2)^{n_3}(q_4^2)^{n_4}$ with $n_t + n_3 + n_4 \leq 4$ denoted by \star . Lower panels display the relative difference with respect to the exact result.

In Fig. 2 we show the real and imaginary parts of the two helicity amplitudes $\mathcal{A}_{++++}^{(0)}$ and $\mathcal{A}_{++00}^{(0)}$ for $p_T = 150$ GeV and on-shell Z boson production, i.e., $q_3^2 = q_4^2 = m_Z^2$, as a function of \sqrt{s} . The upper panels show the helicity amplitudes in various approximations and the lower panels the relative deviation to the exact results, i.e. 10^{-2} on the y axis corresponds to a 1% deviation. In each panel we show the exact result as a solid black line. The results from the t expansion are shown as dashed lines. Here we show four curves which correspond to $m_Z^2 = 0$, the inclusion of quadratic terms in m_Z , the inclusion of quartic terms, and the inclusion of the additional higher order terms in m_Z . We show three dash-dotted curves for the high-energy approximation which include either no m_Z^2 term, an expansion up to m_Z^2 or up to m_Z^4 . From Fig. 2 we observe good agreement

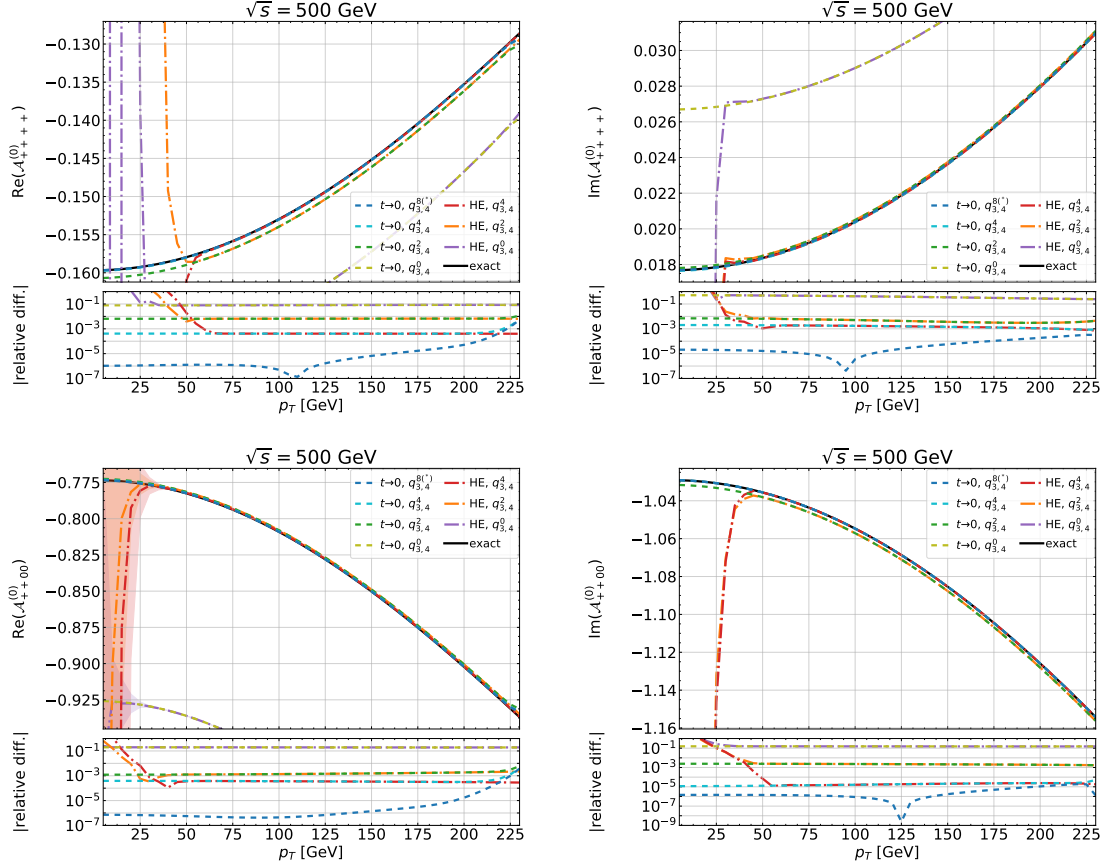


Figure 3: Same as Figure 2 but for fixed $\sqrt{s} = 500$ GeV as a function of p_T .

between the forward and high-energy approximation over the whole range of \sqrt{s} . For $m_Z = 0$ the agreement with the exact result is at the few-percent level. This improves significantly after including the quadratic mass corrections and is well below the percent level once quartic terms are included. The additional m_Z terms which are available for the t expansion provide small additional improvements for the kinematic range chosen in Fig. 2. For lower energies they become more important.

In Fig. 3 we show the helicity amplitudes $\mathcal{A}_{++++}^{(0)}$ and $\mathcal{A}_{++00}^{(0)}$ for fixed $\sqrt{s} = 500$ GeV as a function of p_T . We use the same notation as in Fig. 2. These plots demonstrate that there is a relatively large region for p_T where both approximations agree with the exact results below the per mille level, and for a large part of the phase space even at the level of 10^{-6} . Furthermore, as expected, for small and large p_T there is perfect agreement between the exact results and the t and high-energy expansions, respectively. Note that for small values of p_T the Padé-improved high-energy expansion becomes unstable.

Finally, in Fig. 4 we study the dependence of the expansion accuracy on the virtuality of the final-state momenta q_3 and q_4 . We fix $p_T = 100$ GeV and $\sqrt{s} = 400$ GeV and show,

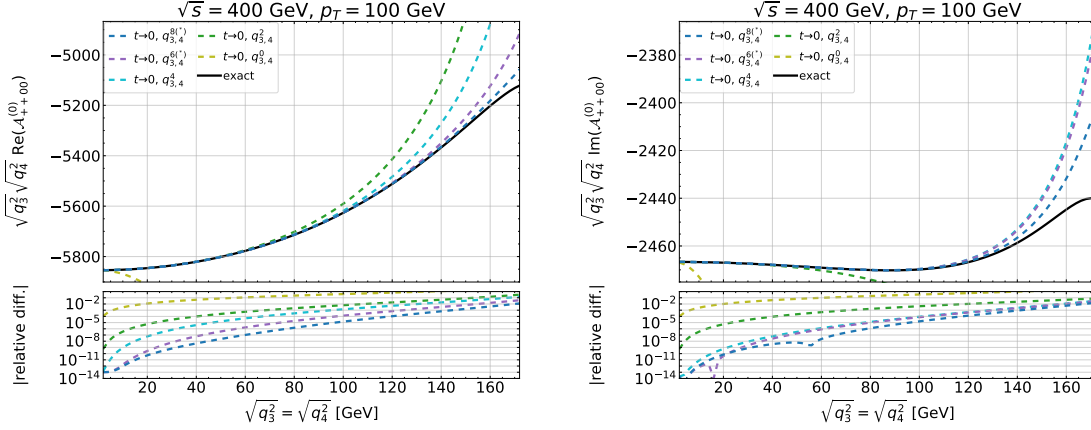


Figure 4: Same as Figure 2 but for fixed $\sqrt{s} = 400$ GeV and $p_T = 100$ GeV as a function of $\sqrt{q_3^2} = \sqrt{q_4^2}$.

for $\mathcal{A}_{++00}^{(0)}$, the dependence on $q_3^2 = q_4^2$. For the chosen values of p_T and \sqrt{s} it is sufficient to consider only the t expansion. To avoid a divergent behaviour for small q_3^2 and q_4^2 we multiply the plotted helicity amplitude by $\sqrt{q_3^2} \sqrt{q_4^2}$. The exact result is shown as black solid lines and the dashed curves include various expansion depths in q_3^2 and q_4^2 . In the lower panel we show the relative differences between the expansions and the exact result. It is impressive that for $q_3^2, q_4^2 \rightarrow 0$ we reproduce more than 10 digits of the exact result after including quartic expansion terms. For $q_3^2 = q_4^2 = m_Z^2$ the agreement is at the level of 10^{-4} and even for $q_3^2 = q_4^2 = (130 \text{ GeV})^2$ the agreement with the exact result is of the order of 0.1% for the real and about a factor 10 better for the imaginary part. The agreement is similar for all other helicity amplitudes.

3.3 Two-loop results to $gg \rightarrow Z^* Z^*$

Next, we perform a similar comparison at the two-loop level where we study the differences between the forward and high-energy expansions and the convergence of the $q_{3,4}^2$ series. In Fig. 5 we show the real and imaginary parts of $\mathcal{A}_{++++}^{(1)}$ and $\mathcal{A}_{++00}^{(1)}$ for fixed $p_T = 150$ GeV as a function of \sqrt{s} . The same notation as in the corresponding one-loop plots is used (see Fig. 2; this time no exact results are shown). The lower panels show the relative difference to the best available approximation from the forward expansion (shown as dark blue curve in the top panels). We observe a similar pattern as at one-loop order. There is a good agreement between the $t \rightarrow 0$ and high-energy expansion. Furthermore, in general the quartic corrections in the final-state masses provide contributions in the sub-percent level which suggests a good convergence.

In Fig. 6 we fix $\sqrt{s} = 500$ GeV and vary p_T . In all cases we observe an intermediate region for p_T where both expansions agree at the sub-percent level. For small values of p_T the

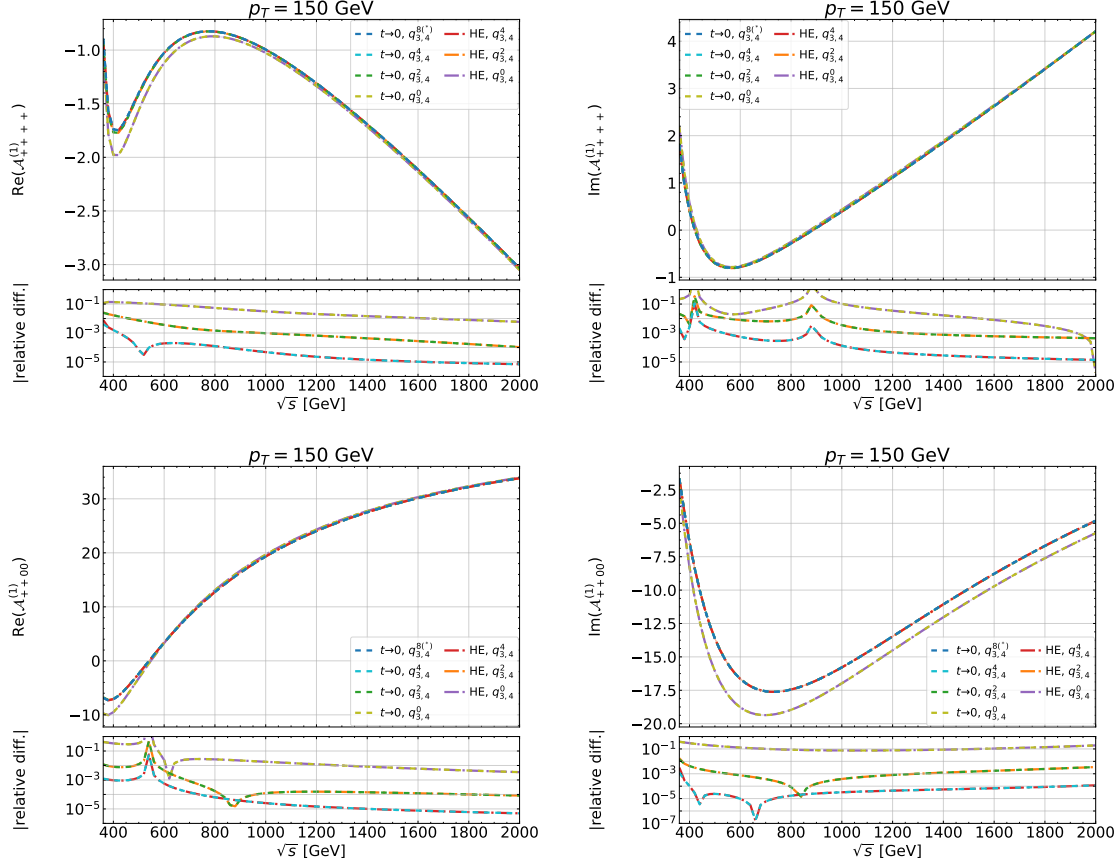


Figure 5: Real and imaginary parts of $\mathcal{A}_{++++}^{(1)}$ and $\mathcal{A}_{++00}^{(1)}$ as a function of \sqrt{s} for $p_T = 150$ GeV and $q_3^2 = q_4^2 = m_Z^2$. High energy and $t \rightarrow 0$ expansions are shown including mass corrections up to $q_{3,4}^{\{0,2,4\}}$. Also shown are higher mass corrections up to $q_{3,4}^8$ for the $t \rightarrow 0$ expansion with fewer expansion terms in t according to $t^{n_t}(q_3^2)^{n_3}(q_4^2)^{n_4}$ with $n_t + n_3 + n_4 \leq 4$ denoted by \star . Lower panels display the relative difference with respect to the best approximation of the $t \rightarrow 0$ expansion.

Padé procedure applied to the high-energy approximation produces large uncertainties. On the other hand, for large p_T the forward expansion becomes unstable as can be seen on the very right of the plots.

In Fig. 6 we also show the results from the p_T expansion computed in Ref. [19]. We observe good agreement at the level of 10^{-3} or below between the t and p_T expansion. For larger values of \sqrt{s} (not shown in Fig. 6), which allows for larger values of p_T , the results from Ref. [19] diverge earlier than the results obtained in the current paper, which includes a much deeper expansion.

In Fig. 7 we show for $\sqrt{q_3^2}\sqrt{q_4^2}\mathcal{A}_{++00}$ the dependence on $\sqrt{q_3^2} = \sqrt{q_4^2}$ for $p_T = 100$ GeV and $\sqrt{s} = 400$ GeV. We show results for the t expansion (which for this phase-space

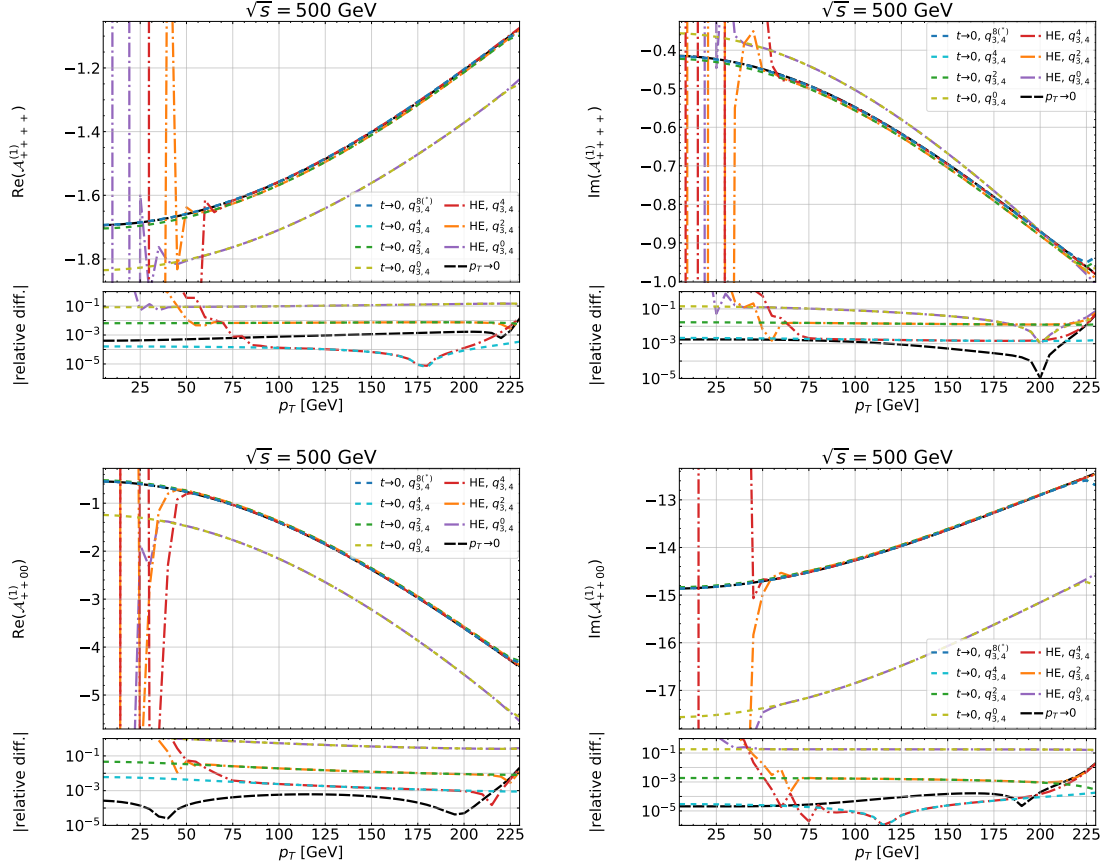


Figure 6: Same as Figure 5 but for fixed $\sqrt{s} = 500$ GeV as a function of p_T .

point is the appropriate choice) including different orders in q_3^2 and q_4^2 . In the lower panel the relative difference to the best approximation is considered. In the whole range of $\sqrt{q_3^2} = \sqrt{q_4^2}$ we observe a rapid convergence of our expansions which suggests that for small $\sqrt{q_3^2} = \sqrt{q_4^2}$ we have a precision of more than 10 digits which reduces to about 5 digits for $\sqrt{q_3^2} = \sqrt{q_4^2} = m_Z$ and 3 digits (or better) for $\sqrt{q_3^2} = \sqrt{q_4^2} = 130$ GeV. Thus, our results conveniently cover the whole range including off-shell Z boson pair production with a virtuality in the vicinity of the Higgs boson mass.

3.4 Finite virtual corrections for $gg \rightarrow Z^* Z^*$

In analogy to double Higgs boson production (see, e.g., Refs. [38, 55]) we define the finite, virtual contribution to the cross section as [16]

$$\tilde{\mathcal{V}}_{\text{fin}}^{ZZ} = \frac{1}{64} \left(\frac{\alpha_s}{2\pi} \right)^2 \sum_{\lambda_1, \lambda_2, \lambda_3, \lambda_4} \left[C_{\lambda_1 \lambda_2 \lambda_3 \lambda_4} + \left(\tilde{\mathcal{A}}_{\lambda_1 \lambda_2 \lambda_3 \lambda_4}^{(0)*} \tilde{\mathcal{A}}_{\lambda_1 \lambda_2 \lambda_3 \lambda_4}^{(1)} + \tilde{\mathcal{A}}_{\lambda_1 \lambda_2 \lambda_3 \lambda_4}^{(0)} \tilde{\mathcal{A}}_{\lambda_1 \lambda_2 \lambda_3 \lambda_4}^{(1)*} \right) \right],$$

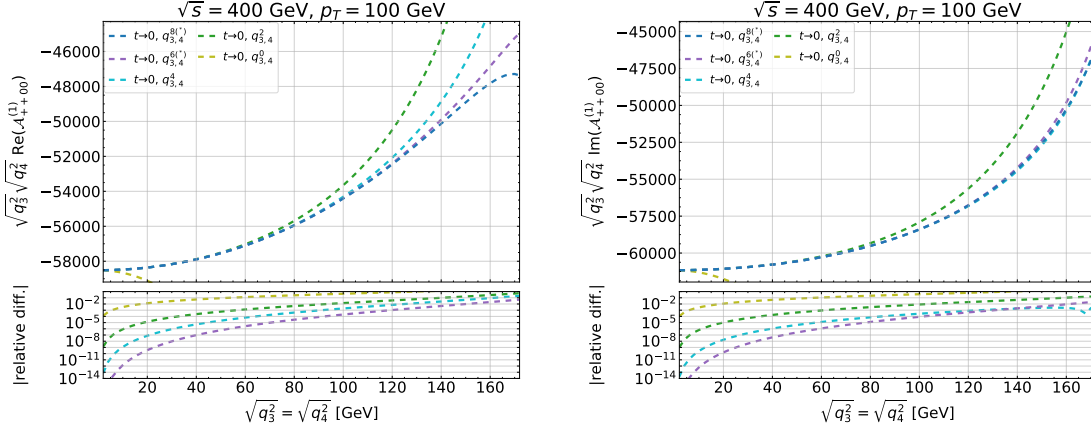


Figure 7: Same as Figure 2 but for fixed $\sqrt{s} = 400$ GeV and $p_T = 100$ GeV as a function of $\sqrt{q_3^2} = \sqrt{q_4^2}$. Here, the relative difference is plotted with respect to the $q_{3,4}^{8(*)}$ curve.

(29)

where $C_{\lambda_1 \lambda_2 \lambda_3 \lambda_4}$ is defined by

$$C_{\lambda_1 \lambda_2 \lambda_3 \lambda_4} = \left| \tilde{\mathcal{A}}_{\lambda_1 \lambda_2 \lambda_3 \lambda_4}^{(0)} \right|^2 C_A \left(\pi^2 - \log^2 \frac{\mu_r^2}{s} \right) \quad (30)$$

and $\tilde{\mathcal{A}}_{\lambda_1 \lambda_2 \lambda_3 \lambda_4}^{\{(0),(1)\}}$ are the corresponding one-loop and two-loop ultra-violet finite and infra-red subtracted helicity amplitudes evaluated at $\mu^2 = -s$ such that the μ_r^2 dependence of $\tilde{\mathcal{V}}_{\text{fin}}^{ZZ}$ is contained in $\alpha_s(\mu_r) \equiv \alpha_s^{(5)}(\mu_r)$ and the quantities $C_{\lambda_1 \lambda_2 \lambda_3 \lambda_4}$. For convenience we introduce the quantity

$$\mathcal{V}_{\text{fin}}^{ZZ} = \frac{\tilde{\mathcal{V}}_{\text{fin}}^{ZZ}}{\alpha_s^2}. \quad (31)$$

In Fig. 8 we compare results for $\mathcal{V}_{\text{fin}}^{ZZ}$ with $\mu_r^2 = s$ obtained on the basis of our expansions to numerical results from Refs. [21, 23] based on pySecDec [56–58] as a ratio $\mathcal{V}_{\text{fin}}^{ZZ, \text{exp}} / \mathcal{V}_{\text{fin}}^{ZZ, \text{num}}$. The plot contains 132 data points over a broad range of p_T and \sqrt{s} . For the construction of $\mathcal{V}_{\text{fin}}^{ZZ, \text{exp}}$ we use the exact one-loop amplitudes and all available expansion terms for the two-loop helicity amplitudes. The orange dots correspond to the t expansion including the expansion depth described in Section 2.3.2. To obtain the green dots we additionally include all terms with $n_t + n_3 + n_4 \leq 5$ for \mathcal{A}_{++00} , which provides the numerically dominant contribution. The improvement is clearly visible. The results of the high-energy expansion are shown as red dots. We find, for all data points, an agreement below 0.02%. Below $p_T = 210$ GeV, where we use the $t \rightarrow 0$ expansion, we find an agreement of at least 0.005% as can be seen from Fig. 9. From this plot one can see that $\mathcal{V}_{\text{fin}}^{ZZ, \text{exp}}$ approximates the exact result impressively well.

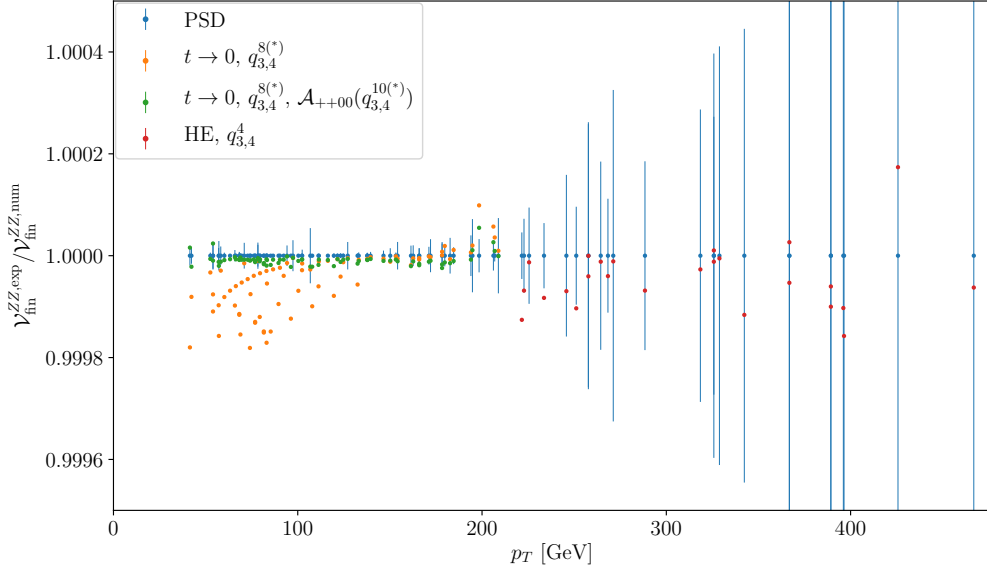


Figure 8: Ratio $\mathcal{V}_{\text{fin}}^{ZZ,\text{exp}} / \mathcal{V}_{\text{fin}}^{ZZ,\text{num}}$ as a function of p_T . In the high-energy region terms up to order m_t^{100} are included. For $t \rightarrow 0$ terms up to order t^{10} for $q_{3,4}^{\{0,2,4\}}$ and $q_{3,4}^6$ and $q_{3,4}^8$ with a lower expansion depth in t terms are included. In addition, results for $t \rightarrow 0$ are also shown with \mathcal{A}_{++00} up to $q_{3,4}^{10}$ with a lower expansion depth in t . The reference values denoted by “PSD” are obtained from Refs. [21, 23].

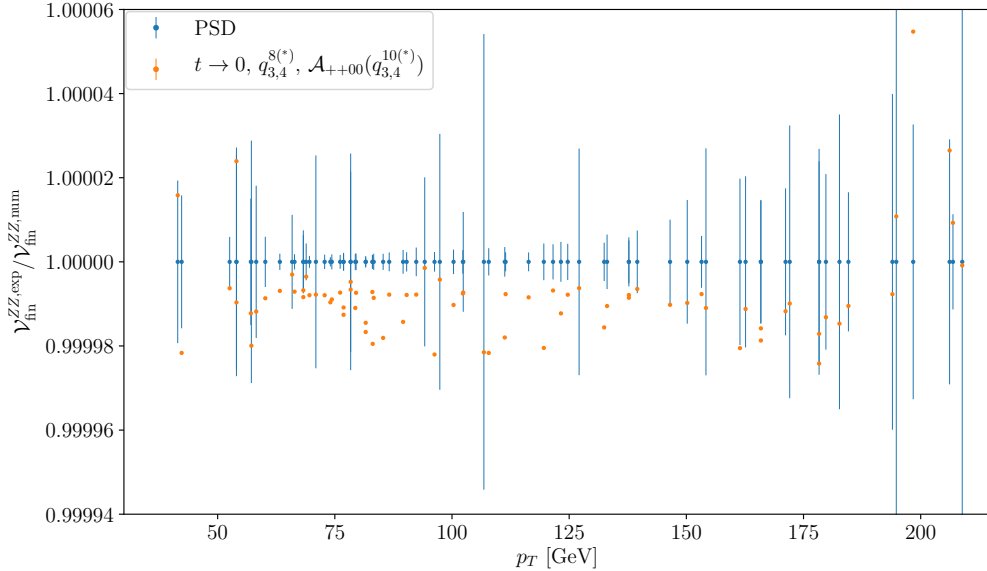


Figure 9: Magnification of data shown in Fig. 8 for $p_T \leq 210$ GeV. Results are shown for the best approximation of the $t \rightarrow 0$ expansion. The reference values denoted by “PSD” are obtained from Refs. [21, 23].

3.5 Two-loop results for $gg \rightarrow \gamma\gamma$

Our amplitudes for $gg \rightarrow Z^*Z^*$ can also be used to obtain results for the process $gg \rightarrow \gamma\gamma$ by setting

$$v_t \rightarrow eQ_t, \quad a_t \rightarrow 0, \quad q_3^2 = q_4^2 = 0. \quad (32)$$

The triangle and double triangle contributions vanish in this case. For on-shell photon production the helicity amplitudes in Eq. (24) with $\lambda_i = 0$ vanish and we are left with the eight helicity amplitudes, which can be reduced to four linearly independent ones using the symmetries in Eq. (25).

The two-loop amplitudes have been calculated before with numerical methods in Refs. [29, 59, 60]. More recently, analytic results have also become available [31, 32]. The full process of di-photon production involving an internal heavy top quark also has contributions from $q\bar{q}$ initial states, for which we do not provide amplitudes.

For illustration we show in Fig. 10 the two-loop results for the helicity amplitude \mathcal{A}_{++++} for fixed- p_T (top panels) and fixed- \sqrt{s} (bottom panels). They show a similar behaviour as the corresponding plots for $gg \rightarrow ZZ$ (see Figs. 5 and 6). Note, however, that the agreement between the high-energy and $t \rightarrow 0$ expansion is significantly better and reaches in some case about 10 digits as can be seen in the plots showing the relative difference. This improvement is due to the fact that the expansion in q_3^2 and q_4^2 , which limits the accuracy of the approximation, is not required in this case.

We note that our results can readily be used to consider off-shell photon production by considering $q_3^2, q_4^2 \neq 0$. Since we have a joint expansion in q_3^2 and q_4^2 the photons cannot be arbitrarily off-shell. However, we know that the expansion provides precise results at least up to $q_3^2, q_4^2 \sim (125 \text{ GeV})^2$ from the $gg \rightarrow HH$ [24] and $gg \rightarrow Z^*Z^*$ (see Fig. 7) amplitudes. We expect the quality of the expansion to behave similarly to the one shown in Figs. 4 and 7, which suggest that we, approximately, lose about one digit of accuracy for every 20 GeV increase in q_3^2 and q_4^2 . In this case the full set of helicity amplitudes (see Eq. (21)) contributes.

3.6 Two-loop results for $gg \rightarrow Z\gamma$

The amplitudes for $gg \rightarrow Z^*Z^*$ can additionally be used to obtain results for the process $gg \rightarrow Z\gamma$, where one or both final state bosons are either on- or off-shell. Here we have to set

$$v_t^2 \rightarrow \frac{e^2 Q_t}{2s_w c_w} (I_t^3 - 2Q_t s_w^2), \quad a_t^2 \rightarrow 0. \quad (33)$$

The triangle and double triangle contributions also vanish in this case. For on-shell photon production the helicity amplitudes in Eq. (24) with $\lambda_4 = 0$ vanish.

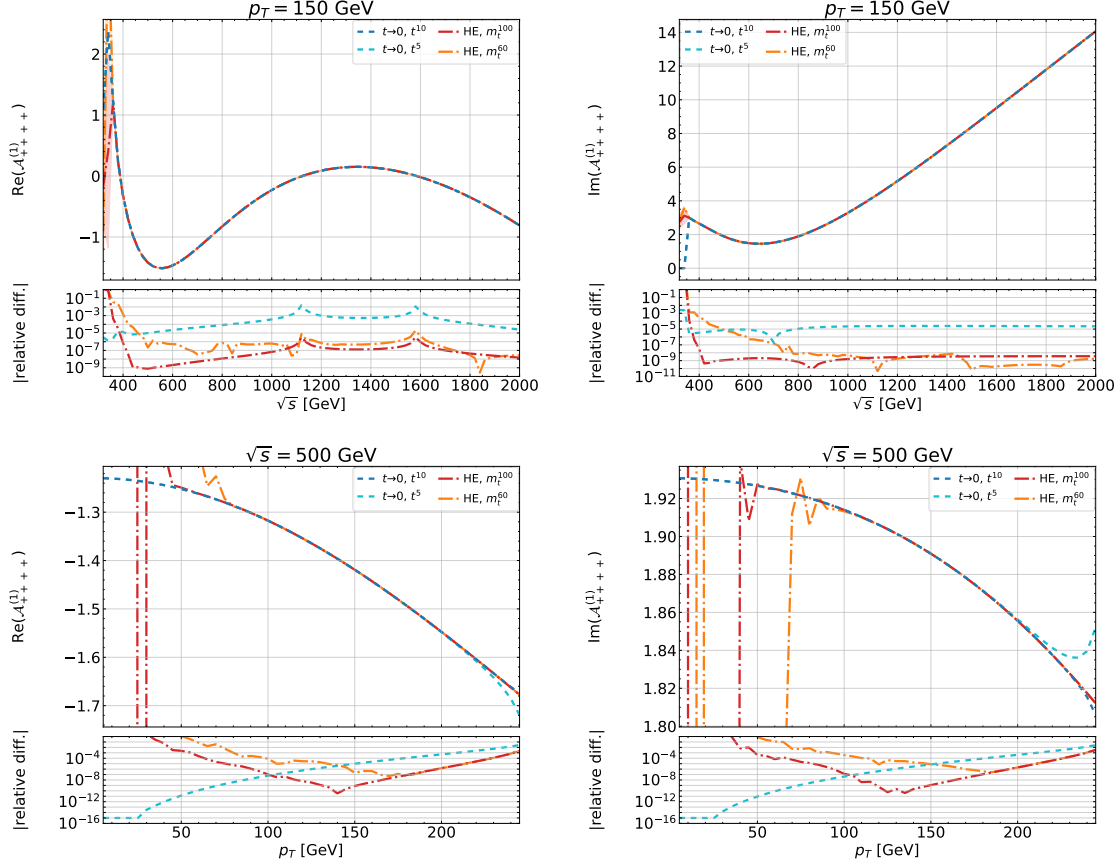


Figure 10: Real and imaginary parts of $\mathcal{A}_{++++}^{(1)}$ for $gg \rightarrow \gamma\gamma$ for $p_T = 150$ GeV as a function of \sqrt{s} and for $\sqrt{s} = 500$ GeV as a function of p_T . High-energy and $t \rightarrow 0$ expansions are shown with expansions terms up to $m_t^{\{60,100\}}$ and $t^{\{5,10\}}$, respectively. Lower panels display the relative difference with respect to the best approximation of the $t \rightarrow 0$ expansion.

The process mediated by massless quarks has been calculated in Refs. [61–63] and matched to parton showers in Refs. [64,65]. In the latter case the gluon fusion channel was found to be small, cf. Ref. [62], and neglected for the numerical studies. It would be interesting to study the impact of massive quarks on the differential distributions.

We show the result for the two-loop contributions to the helicity amplitude \mathcal{A}_{++++} in Fig. 11 for illustration.

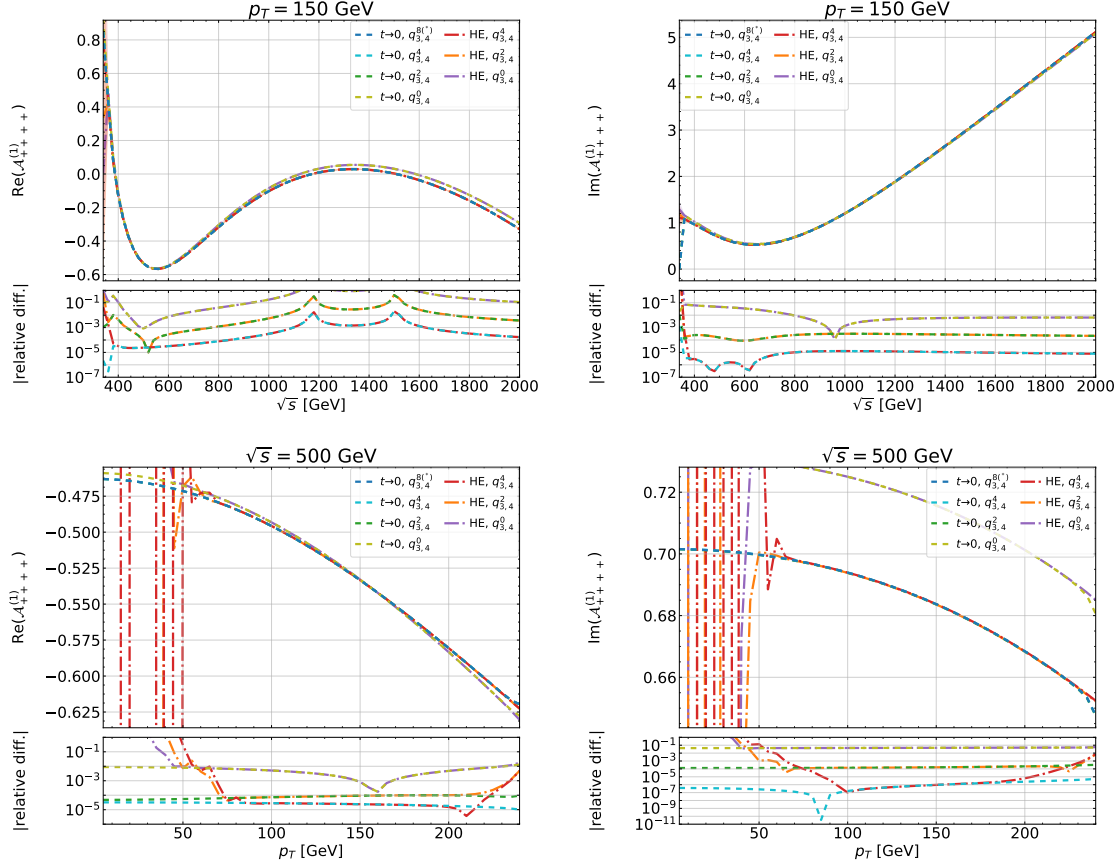


Figure 11: Real and imaginary parts of $\mathcal{A}_{++++}^{(1)}$ for $gg \rightarrow Z\gamma$ for $p_T = 150$ GeV as a function of \sqrt{s} and for $\sqrt{s} = 500$ GeV as a function of p_T . High-energy and $t \rightarrow 0$ expansions are shown including mass corrections up to $q_{3,4}^{\{0,2,4\}}$. Also shown are higher mass corrections up to $q_{3,4}^8$ for the $t \rightarrow 0$ expansion with fewer expansion terms in t according to $t^{n_t}(q_3^2)^{n_3}(q_4^2)^{n_4}$ with $n_t + n_3 + n_4 \leq 4$ denoted by \star . Lower panels display the relative difference with respect to the best approximation of the $t \rightarrow 0$ expansion.

4 $gg \rightarrow ZH$

4.1 Amplitude

We decompose the amplitude for $g(q_1)g(q_2) \rightarrow Z(q_3)H(q_4)$ as a linear combination of form factors [8],

$$\begin{aligned}
A(q_1, q_2, q_3) &= i\delta_{ab} \frac{\sqrt{2}G_F m_Z}{s} \frac{\alpha_s(\mu)}{\pi} A^{\mu\nu\rho}(q_1, q_2, q_3) \epsilon_\mu^a(q_1) \epsilon_\nu^b(q_2) \epsilon_\rho^*(q_3), \\
A^{\mu\nu\rho}(q_1, q_2, q_3) &= \\
&\left\{ \left(\frac{s}{2} \varepsilon^{\mu\nu\rho\alpha} q_{2\alpha} - q_2^\mu \varepsilon^{\nu\rho\alpha\beta} q_{1\alpha} q_{2\beta} \right) F_1(t, u) - \left(\frac{s}{2} \varepsilon^{\mu\nu\rho\alpha} q_{1\alpha} - q_1^\nu \varepsilon^{\mu\rho\alpha\beta} q_{1\alpha} q_{2\beta} \right) F_1(u, t) \right. \\
&+ \left(q_3^\mu + \frac{m_Z^2 - t}{s} q_2^\mu \right) \varepsilon^{\nu\rho\alpha\beta} q_{2\alpha} [q_{1\beta} F_2(t, u) + q_{3\beta} F_3(t, u)] \\
&+ \left(q_3^\nu + \frac{m_Z^2 - u}{s} q_1^\nu \right) \varepsilon^{\mu\rho\alpha\beta} q_{1\alpha} [q_{2\beta} F_2(u, t) + q_{3\beta} F_3(u, t)] \\
&\left. + \left(\frac{s}{2} \varepsilon^{\mu\nu\rho\alpha} q_{3\alpha} - q_2^\mu \varepsilon^{\nu\rho\alpha\beta} q_{1\alpha} q_{3\beta} + q_1^\nu \varepsilon^{\mu\rho\alpha\beta} q_{2\alpha} q_{3\beta} + g^{\mu\nu} \varepsilon^{\rho\alpha\beta\gamma} q_{1\alpha} q_{2\beta} q_{3\gamma} \right) F_4(t, u) \right\}. \quad (34)
\end{aligned}$$

and use on-shell kinematics⁶ specified in Section 2.1.

We follow Ref. [13] and discuss the results for the six independent form factors

$$F_{12}^+(t, u), F_{12}^-(t, u), F_2^-(t, u), F_3^+(t, u), F_3^-(t, u), F_4(t, u) \quad (35)$$

that can be obtained after taking linear combinations of those of Eq. (34):

$$\begin{aligned}
F_2^-(t, u) &= F_2(t, u) - F_2(u, t), & F_2^+(t, u) &= F_2(t, u) + F_2(u, t), \\
F_{12}^-(t, u) &= F_{12}(t, u) - F_{12}(u, t), & F_{12}^+(t, u) &= F_{12}(t, u) + F_{12}(u, t), \\
F_3^-(t, u) &= F_3(t, u) - F_3(u, t), & F_3^+(t, u) &= F_3(t, u) + F_3(u, t), \quad (36)
\end{aligned}$$

where

$$\begin{aligned}
F_{12}(t, u) &= F_1(t, u) - \frac{t - m_Z^2}{s} F_2(t, u), \\
F_{12}(u, t) &= F_1(u, t) - \frac{u - m_Z^2}{s} F_2(u, t). \quad (37)
\end{aligned}$$

In the following, we only discuss the results for box diagrams. The triangle diagrams only contribute to F_{12}^+ . The contribution from double-triangle diagrams can be cast into one form factor which is given in the Appendix of Ref. [13].

⁶Our results for the form factors have an explicit dependence on m_Z^2 and m_H^2 and thus they can immediately be applied to the production of off-shell Z and Higgs bosons.

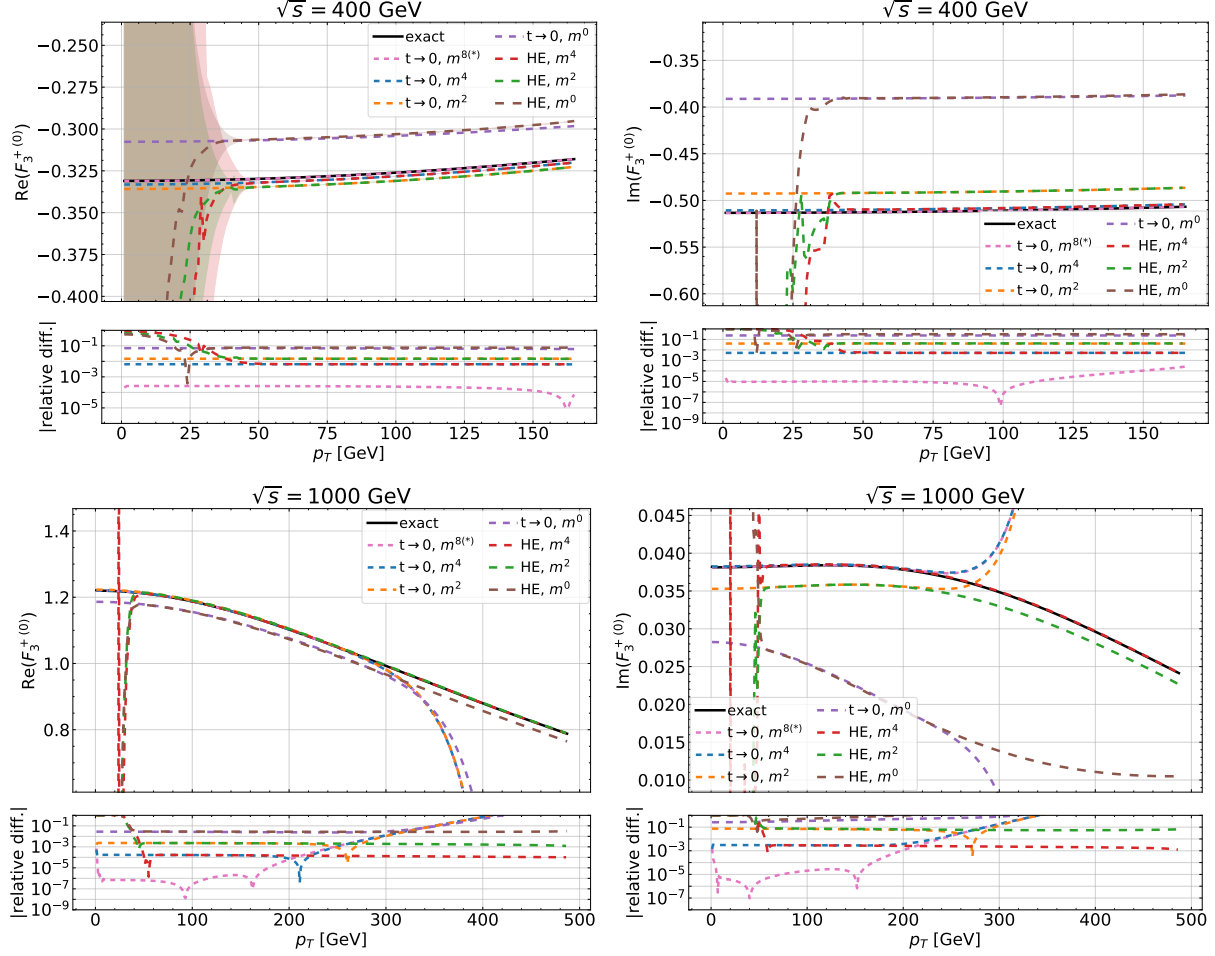


Figure 12: Real and imaginary parts of $F_3^{+(0)}$ as a function of p_T for $\sqrt{s} = \{400, 1000\}$ GeV. High-energy and $t \rightarrow 0$ expansions are shown including mass corrections up to $m_{Z,H}^{\{0,2,4\}}$. Also shown are higher mass corrections up to $m_{Z,H}^8$ for the $t \rightarrow 0$ expansion with fewer expansion terms in t according to $t^{n_t}(m_Z^2)^{n_3}(m_H^2)^{n_4}$ with $n_t + n_3 + n_4 \leq 4$ denoted by \star . The lower panels display the relative difference with respect to the exact result.

4.2 One-loop results for $gg \rightarrow ZH$

In Figs. 12 and 13 we compare our approximations to the exact one-loop results for the real and imaginary parts of the form factor F_3^+ . Similar results are also obtained for all other form factors. The exact one-loop results have been calculated with the `calc` setup without applying any expansions and are expressed in terms of scalar one-loop functions. We use `LoopTools` [66] for their numerical evaluation.

Both in the forward-limit and high-energy approximation we include up to (at least) quartic expansion terms in the final-state Higgs and Z boson masses. Furthermore we

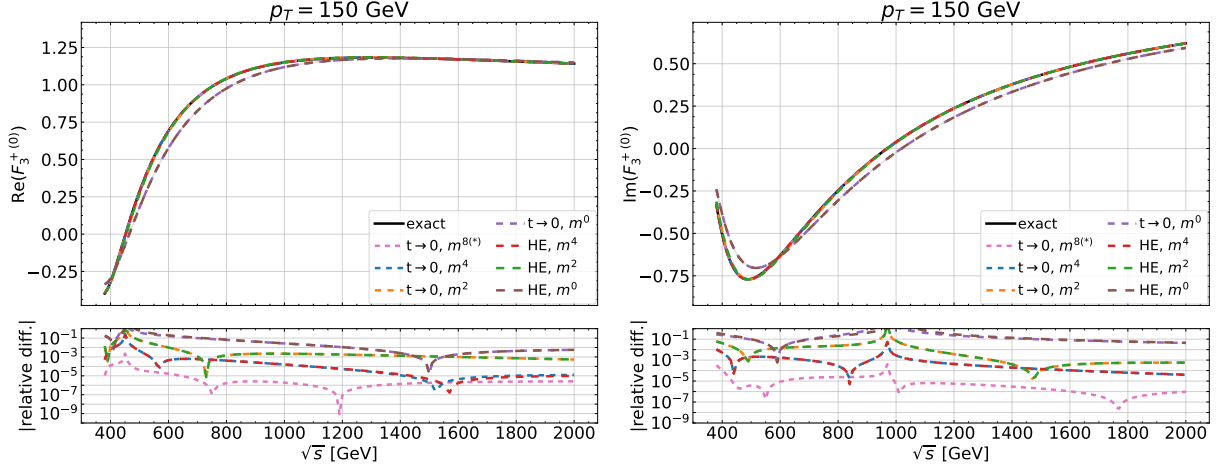


Figure 13: Same as Figure 12 but for fixed $p_T = 150$ GeV as a function of \sqrt{s} .

incorporate expansions up to order t^5 and m_t^{112} , respectively. The high-energy expansion is supplemented by Padé approximations following the procedure outlined in Ref. [16]. For the construction of the Padé approximants we use expansions in m_t between m_t^{98} and m_t^{112} . It provides a central value and an uncertainty for each phase-space point. In the plots, the uncertainty is only visible for low energies; here the t expansion provides precise predictions.

In each plot we show the form factors in the upper panel and in the lower panel the absolute value of the relative difference to the exact result. Both for fixed- \sqrt{s} (cf. Fig. 12) and fixed- p_T (cf. Fig. 13) we observe an agreement with the exact results for the form factor at 0.1% or better. The residual difference mainly comes from the limited expansion depth in m_H and m_Z ; the agreement between the high-energy and t expansion is far below the per mille level in the intermediate regions of p_T and \sqrt{s} , respectively. We remark that the relative difference increases by about a factor 10 in case we drop the quartic terms and only keep the quadratic terms in m_H and m_Z .

From Figs. 12 and 13 it is clear that one can simply switch between the two approximations at some intermediate value for p_T or \sqrt{s} . In practice we will switch for $p_T = 150$ GeV where we find a six-digit agreement between the t -expansion and high-energy results. Note that for $p_T = 150$ GeV the minimal value for \sqrt{s} is sufficiently high such that no additional criterion for \sqrt{s} is needed.

4.3 Two-loop results for $gg \rightarrow ZH$

At two loops, exact results are not available to us for the form factors. Thus, we estimate the quality of our approximation by comparing the forward-limit and high-energy expansions and by varying the expansion depths in t , m_t and the external masses m_H and m_Z .

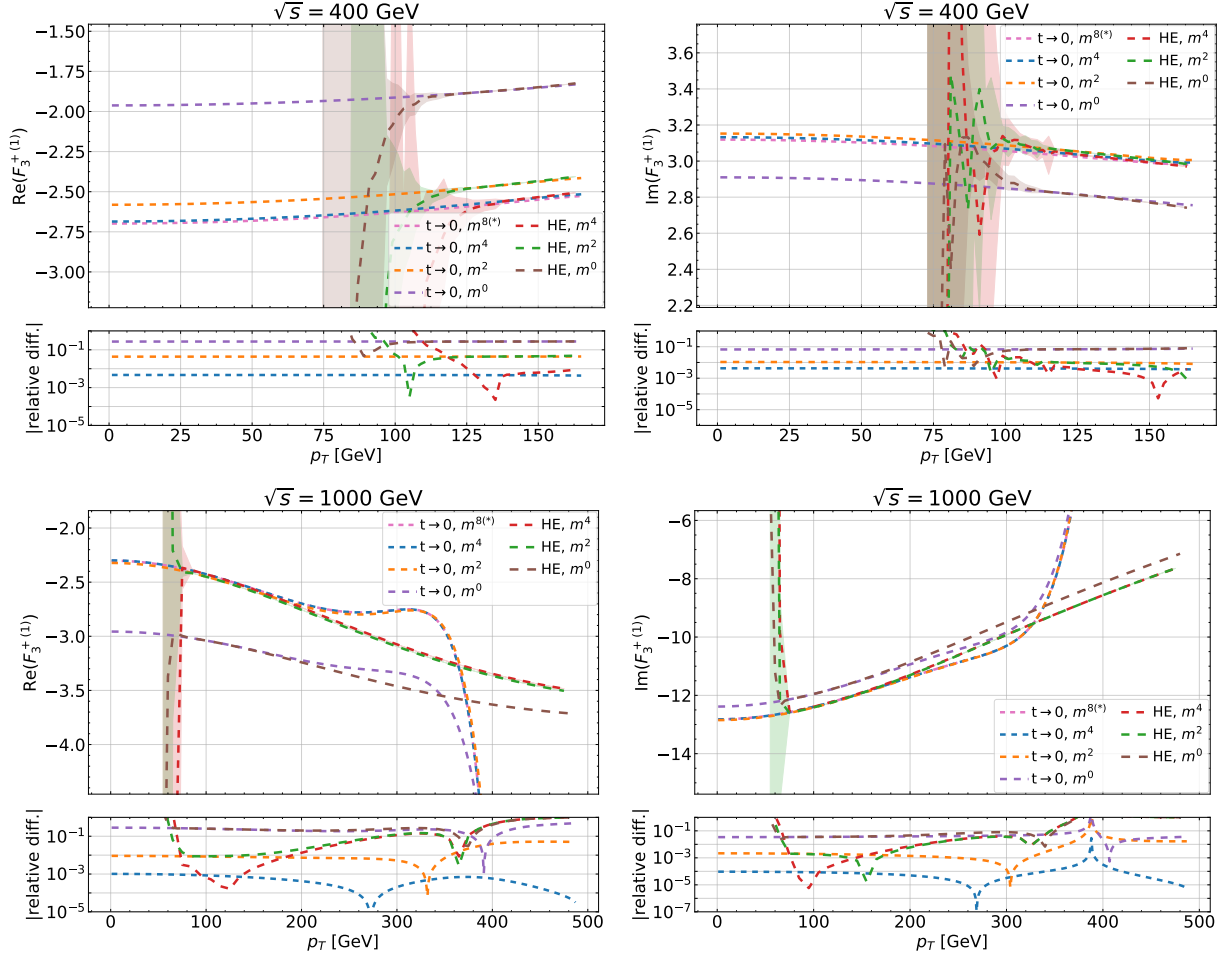


Figure 14: Real and imaginary parts of $F_3^{+, (1)}$ as a function of p_T for $\sqrt{s} = \{400, 1000\}$ GeV. High-energy and $t \rightarrow 0$ expansions are shown including mass corrections up to $m_{Z,H}^{\{0,2,4\}}$. Also shown are higher mass corrections up to $m_{Z,H}^{8(*)}$ for the $t \rightarrow 0$ expansion with fewer expansion terms in t according to $t^{n_t}(m_Z^2)^{n_3}(m_H^2)^{n_4}$ with $n_t + n_3 + n_4 \leq 4$ denoted by \star . The lower panels display the relative difference with respect to the best approximation of the $t \rightarrow 0$ expansion.

In Figs. 14 and 15 we show results for $F_3^{+, (1)}$ for fixed- \sqrt{s} and fixed- p_T , respectively, using the same parameters as in the one-loop plots in the previous subsection. We use t^5 and m_t^{112} terms in the construction of the approximations and show results for massless final-state particles and with quadratic and quartic terms included. One observes a rapid convergence: the difference between the quadratic and quartic results is below 1%. In Fig. 14 we observe that for $p_T \lesssim 125$ GeV the high-energy expansion does not converge. Similarly, for $\sqrt{s} = 1000$ GeV the t expansion is only valid for $p_T \lesssim 300$ GeV. However, for all values of \sqrt{s} both expansions show good agreement for p_T values around 150 GeV, which we use for the transition between the t and high-energy expansions. This is sup-

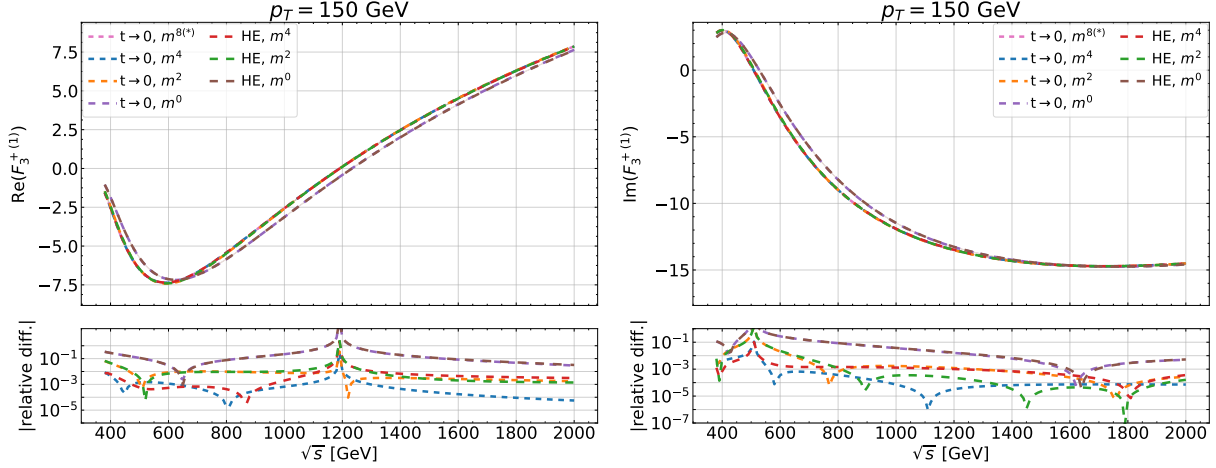


Figure 15: Same as Figure 14 but for fixed $p_T = 150$ GeV as a function of \sqrt{s} .

ported by Fig. 15 which shows an agreement at the level of 10^{-5} . The upwards-oriented kinks originate from zero-crossings of the form factors.⁷ Figs. 14 and 15 show that we are able to cover the whole phase-space by combining our expansions.

4.4 Virtual NLO corrections

For convenience we repeat the formula derived in Ref. [13] for the finite virtual corrections as constructed from the form factors. It is given by⁸

$$\begin{aligned} \tilde{\mathcal{V}}_{\text{fin}}^{ZH} = & \frac{G_F^2 m_Z^2}{4s^2} \left(\frac{\alpha_s}{\pi} \right)^2 \sum_{\lambda_1, \lambda_2, \lambda_3} \left\{ \left[\tilde{A}_{\text{sub}}^{\mu\nu\rho} \tilde{A}_{\text{sub}}^{\star, \mu' \nu' \rho'} \right]^{(1)} + \frac{C_A}{2} \left(\pi^2 - \log^2 \frac{\mu_r^2}{s} \right) \left[\tilde{A}_{\text{sub}}^{\mu\nu\rho} \tilde{A}_{\text{sub}}^{\star, \mu' \nu' \rho'} \right]^{(0)} \right\} \\ & \times \varepsilon_{\lambda_1, \mu}(q_1) \varepsilon_{\lambda_1, \mu'}^*(q_1) \varepsilon_{\lambda_2, \nu}(q_2) \varepsilon_{\lambda_2, \nu'}^*(q_2) \varepsilon_{\lambda_3, \rho}(q_3) \varepsilon_{\lambda_3, \rho'}^*(q_3), \end{aligned} \quad (38)$$

where the form factors entering the amplitude $\tilde{A}_{\text{sub}}^{\mu\nu\rho}$ are the infrared-subtracted finite form factors constructed according to our prescription outlined in Section 2.4, evaluated at $\mu^2 = -s$. The superscripts “(0)” and “(1)” after the square brackets in Eq. (38) indicate that we take the coefficients of $(\alpha_s/\pi)^0$ and $(\alpha_s/\pi)^1$, respectively, of the squared amplitude. For the following discussion it is convenient to introduce the α_s -independent quantity

$$\mathcal{V}_{\text{fin}}^{ZH} = \frac{\tilde{\mathcal{V}}_{\text{fin}}^{ZH}}{\alpha_s^2}. \quad (39)$$

⁷The downwards-oriented kinks in the lower panels of Fig. 15 are at \sqrt{s} values where the expansions cross each other.

⁸As compared to Ref. [13] the formula presented here is multiplied by a factor of four to match the conventions of Ref. [20].

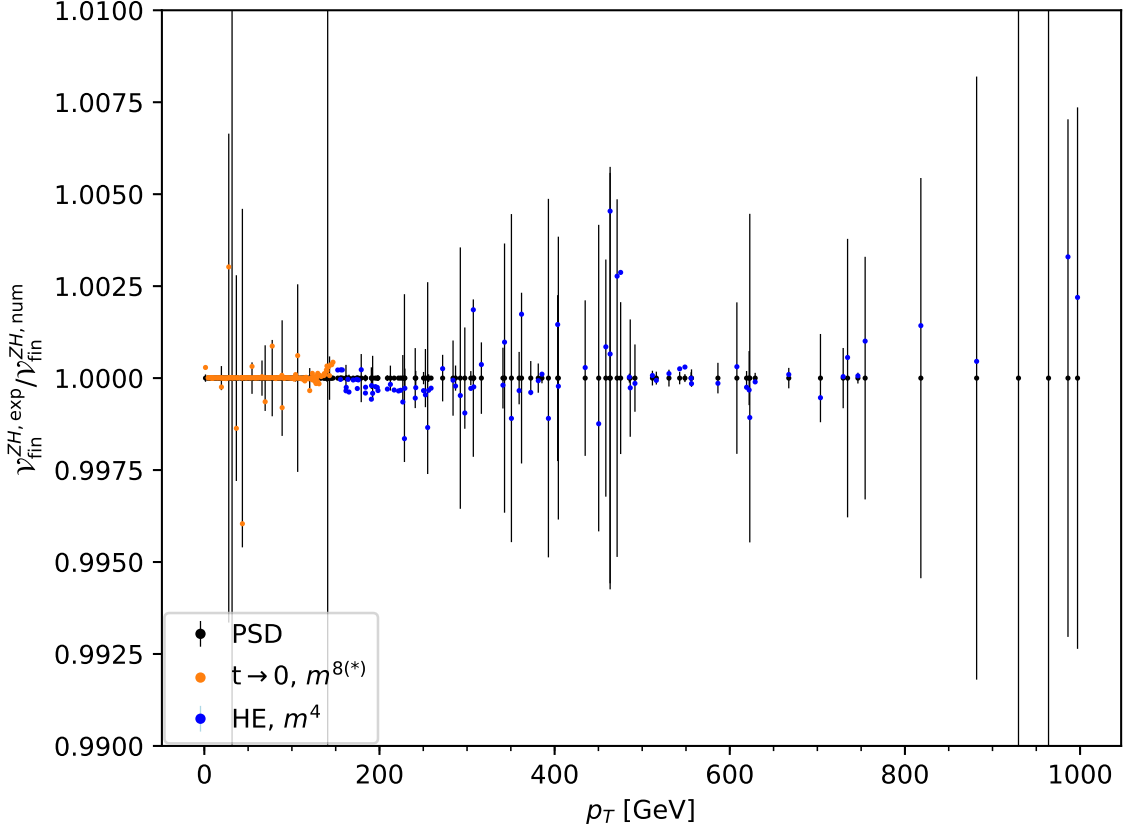


Figure 16: Ratio of $\mathcal{V}_{\text{fin}}^{ZH,\text{exp}}$ and $\mathcal{V}_{\text{fin}}^{ZH,\text{num}}$. In the legend “ m^4 ” refers to the inclusion of quartic terms in m_Z and m_H and in “ m^{8*} ” all available mass terms are included; “HE” stands for the high-energy expansion and “PSD” refers to the results from Ref. [20] based on pySecDec.

$\mathcal{V}_{\text{fin}}^{ZH}$ has been computed in the high-energy limit in Ref. [13] and using a numerical approach in Ref. [20]. A first comparison is available in Fig. 2 of Ref. [22]. We are now in a position to update this plot in two ways. First, we considerably extend the depth of the high-energy expansion from 32 to over 100 terms in m_t . Additionally, we also use the t expansion for the form factors as discussed in the previous subsections. For the construction of $\mathcal{V}_{\text{fin}}^{ZH}$ we use the exact one loop amplitude and all available expansion terms of our analytical approximations for the NLO contribution to the form factors.

In Fig. 16 we compare our predictions for $\mathcal{V}_{\text{fin}}^{ZH}$ with $\mu_r^2 = s$ based on the t and high-energy expansions (shown as orange and blue dots) with results obtained in Ref. [20] with a purely numerical approach (black dots and uncertainty bars) which is based on pySecDec [56–58]. We observe that for most of the data points our analytic expansion approximates the numerical result far below the percent level. In fact, larger deviations are only observed in those cases where the numerical uncertainty is large.

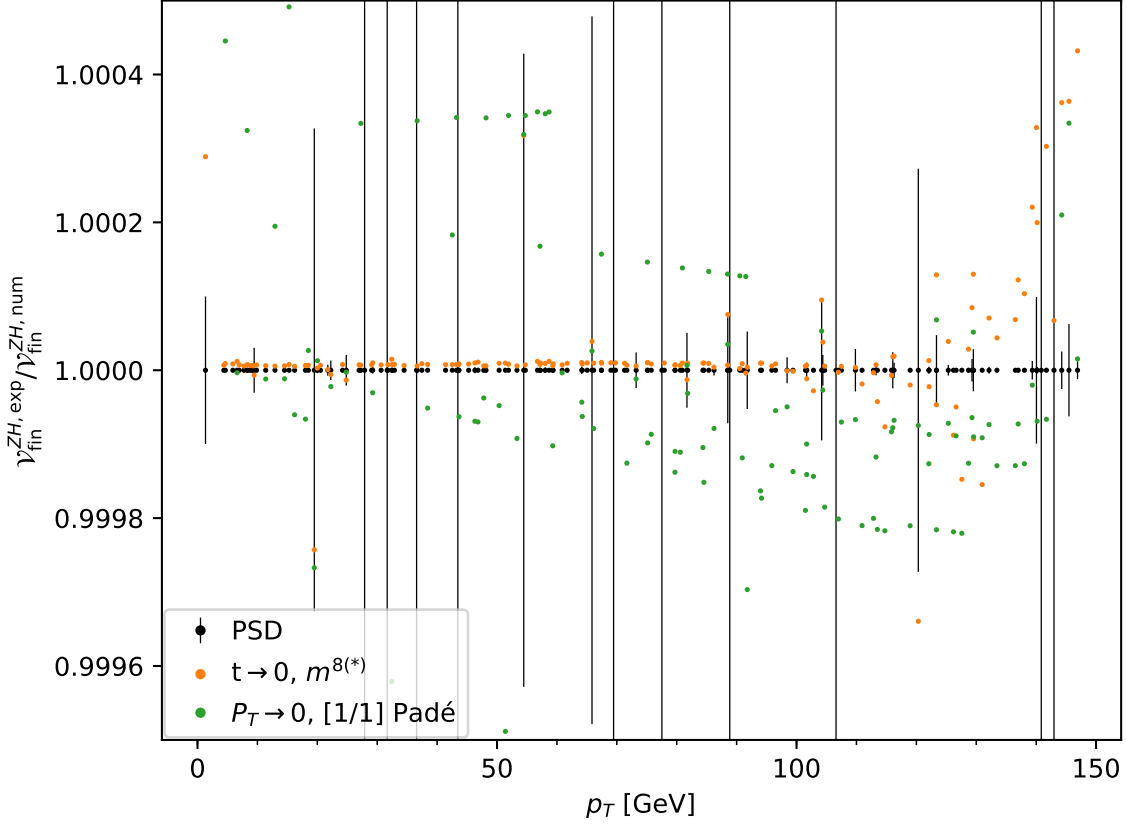


Figure 17: Magnification of Fig. 16 for $p_T \leq 150$ GeV. Note that as compared to Fig. 16 the y axis is blown up by a factor of 20. We also show the results of the p_T expansion from Ref. [28] as green dots. Note that for some phase-space points the p_T expansion results are outside the frame.

To compare in more detail, in Fig. 17 we show a magnification of Fig. 16 for $p_T \leq 150$ GeV. Note that the y axis has been re-scaled by a factor of 20. The results of the Padé-improved p_T expansion from Ref. [28] are shown as green dots. They are less precise; in fact, some of the data points lie outside of the plot area. Note, however, that for phenomenological applications the approximation provided by these points is sufficiently precise.

Finally, we are in the position to present Fig. 18, which is an update of Fig. 2 of Ref. [22] where the numerical results were compared to the high-energy results of Ref. [13]. The comparison included quartic terms in the final-state masses m_Z and m_H . However instead of 112, only 32 expansion terms in m_t were included. Furthermore, at the time Fig. 2 of Ref. [22] was made no t expansion was available. In Fig. 18 we use an expansion up to t^5 .

On the y axis of Fig. 18 we show the quantity

$$\frac{\alpha_s}{4\pi} \frac{\mathcal{V}_{\text{fin}}^{ZH, \text{exp}} - \mathcal{V}_{\text{fin}}^{ZH, \text{num}}}{\mathcal{B}} \quad (40)$$

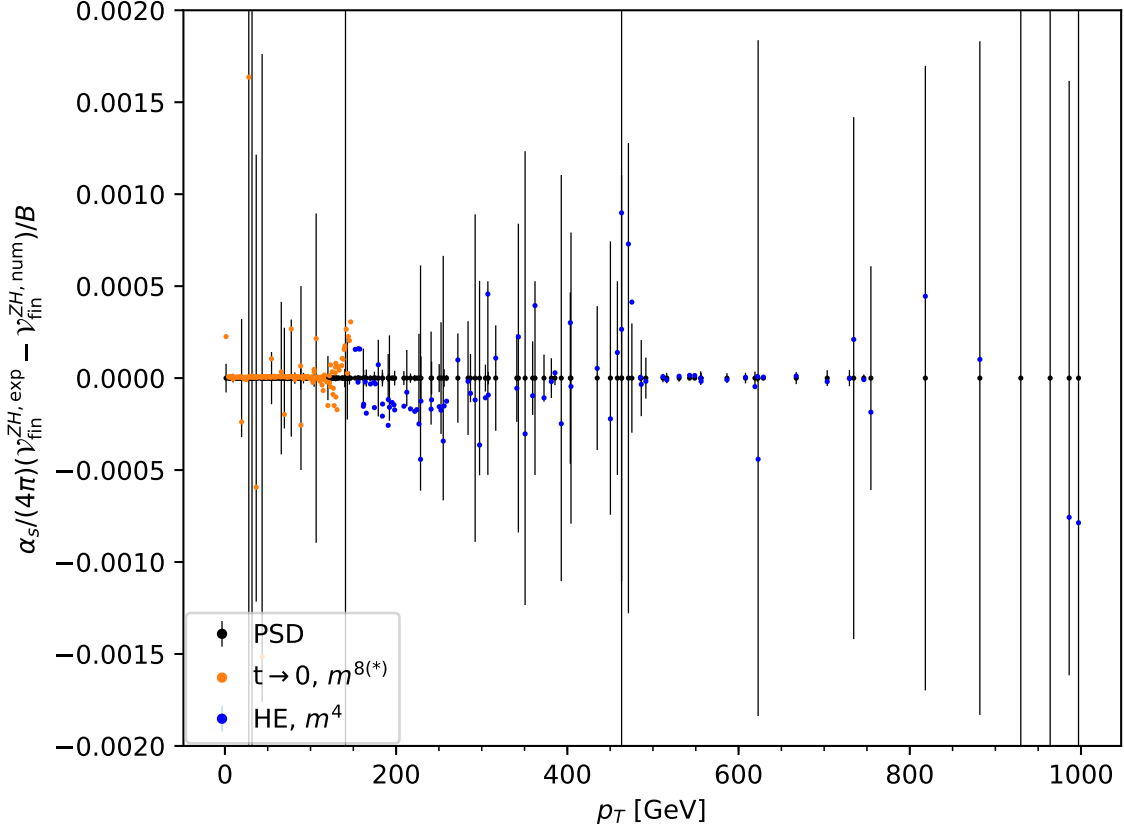


Figure 18: Difference of $\mathcal{V}_{\text{fin}}^{ZH}$ computed from analytic expansion and using a numerical approach. The quantity on the y axis represents the uncertainty at NLO relative to the Born contribution. In the legend “ m^4 ” refers to the inclusion of quartic terms in m_Z and m_H , “HE” stands for the high-energy expansion and “PSD” refers to the results from Ref. [20] based on `pySecDec`.

which quantifies the difference in terms of a typical NLO contribution. Furthermore, it is independent of the infrared subtraction scheme used for removing the infrared singularities. Here, \mathcal{B} is the exact Born contribution and $\mathcal{V}_{\text{fin}}^{ZH,\text{exp}}$ and $\mathcal{V}_{\text{fin}}^{ZH,\text{num}}$ stand for $\mathcal{V}_{\text{fin}}^{ZH}$ obtained with the help of analytic approximations and a numerical approach, respectively. Over the whole p_T range we observe good agreement with the numerical results. Fig. 18 represents an improvement of the results shown in Fig. 2 of Ref. [22] and Fig. 1 of Ref. [67].

In practical applications our expansions have the advantage that they can be evaluated very quickly. We will soon implement them in `ggxy` [68] and expect an evaluation time of a few milli-seconds per phase-space point.

5 Conclusions

In this paper, deep expansions around the forward limit and the high-energy limit have been computed for the processes $gg \rightarrow ZH$ and the top quark contribution to $gg \rightarrow Z^*Z^*$. We have shown that the combination of both expansions covers the whole phase space with very good accuracy. Our analytic results retain explicit dependence on all parameters and it is straightforward to change them and to change the renormalization scheme. This makes them very suitable for the study of off-shell production, since the invariant mass of the final state particles can be changed on-the-fly and no grid has to be computed. Furthermore, their numerical evaluation is very fast. For these reasons, they provide a convenient and practically equivalent alternative to the results obtained with purely numerical methods. In fact, no results for $gg \rightarrow Z^*Z^*$ have been calculated in the literature so far, not even with a numerical approach. As a by-product to the calculation of the top-quark contribution to $gg \rightarrow Z^*Z^*$ we obtain the corresponding results for $gg \rightarrow \gamma^*\gamma^*$ and $gg \rightarrow Z^*\gamma^*$.

As compared to previously known expansion based results for on-shell $gg \rightarrow ZZ$ [19] and $gg \rightarrow ZH$ [28] our expansions are much deeper and thus more precise. We compare the virtual NLO corrections to numerical results [20, 21, 23] and observe agreement below the per mille level, and for small values of t even better. We will implement the results obtained in this paper into the C++ library `ggxy` [68]. This allows for a convenient and flexible way to evaluate the form factors, helicity amplitudes and virtual NLO corrections.

Acknowledgements

This research was supported by the Deutsche Forschungsgemeinschaft (DFG, German Research Foundation) under grant 396021762 — TRR 257 “Particle Physics Phenomenology after the Higgs Discovery”. The work of K. S. was supported by the European Research Council (ERC) under the European Union’s Horizon 2020 research and innovation programme grant agreement 101019620 (ERC Advanced Grant TOPUP) and the UZH Postdoc Grant, grant no. [FK-24-115]. The work of J. D. was supported by STFC Consolidated Grant ST/X000699/1. We thank Stephen Jones and Matthias Kerner for providing numerical results for the virtual-finite cross sections.

A Projectors for $gg \rightarrow Z^*Z^*$

For the helicity amplitude \mathcal{A}_{++00} the coefficients $a_{\lambda_1\lambda_2\lambda_3\lambda_4}^{(i)}$ in Eq. (15) are given by

$$\begin{aligned} a_{++00}^{(1)} &= a_{++00}^{(2)} = a_{++00}^{(3)} = a_{++00}^{(8)} = a_{++00}^{(9)} = a_{++00}^{(10)} = 0, \\ a_{++00}^{(11)} &= a_{++00}^{(12)} = a_{++00}^{(13)} = a_{++00}^{(14)} = a_{++00}^{(15)} = a_{++00}^{(16)} = 0, \end{aligned}$$

$$a_{++00}^{(4)} = a_{++00}^{(5)} = a_{++00}^{(6)} = a_{++00}^{(7)} = \frac{2q_3^2 q_4^2}{\beta^2(d-3)s^3\sqrt{q_3^2}\sqrt{q_4^2}} ,$$

$$a_{++00}^{(17)} = a_{++00}^{(18)} = a_{++00}^{(19)} = a_{++00}^{(20)} = \frac{2(d-4)q_3^2 q_4^2}{\beta^2(d-3)s\sqrt{q_3^2}\sqrt{q_4^2}(q_3^2(q_4^2-t) + t(-q_4^2+s+t))} ,$$

with $d = 4 - 2\epsilon$. The corresponding coefficients for all helicity amplitudes can be found in Ref. [53].

References

- [1] LHC HIGGS CROSS SECTION WORKING GROUP collaboration, *Handbook of LHC Higgs Cross Sections: 4. Deciphering the Nature of the Higgs Sector*, CERN Yellow Rep. Monogr. **2** (2017) 1 [1610.07922].
- [2] O. Brein, R. V. Harlander and T. J. E. Zirke, *vh@nnlo - Higgs Strahlung at hadron colliders*, Comput. Phys. Commun. **184** (2013) 998 [1210.5347].
- [3] ATLAS collaboration, *Measurements of WH and ZH production with Higgs boson decays into bottom quarks and direct constraints on the charm Yukawa coupling in 13 TeV pp collisions with the ATLAS detector*, JHEP **04** (2025) 075 [2410.19611].
- [4] CMS collaboration, *Measurement of simplified template cross sections of the Higgs boson produced in association with W or Z bosons in the $H \rightarrow b\bar{b}$ decay channel in proton-proton collisions at $s=13$ TeV*, Phys. Rev. D **109** (2024) 092011 [2312.07562].
- [5] N. Kauer and G. Passarino, *Inadequacy of zero-width approximation for a light Higgs boson signal*, JHEP **08** (2012) 116 [1206.4803].
- [6] F. Caola and K. Melnikov, *Constraining the Higgs boson width with ZZ production at the LHC*, Phys. Rev. D **88** (2013) 054024 [1307.4935].
- [7] J. M. Campbell, R. K. Ellis and C. Williams, *Bounding the Higgs Width at the LHC Using Full Analytic Results for $gg \rightarrow e^-e^+\mu^-\mu^+$* , JHEP **04** (2014) 060 [1311.3589].
- [8] B. A. Kniehl, *Associated Production of Higgs and Z Bosons From Gluon Fusion in Hadron Collisions*, Phys. Rev. D **42** (1990) 2253.
- [9] D. A. Dicus and C. Kao, *Higgs Boson - Z^0 Production From Gluon Fusion*, Phys. Rev. D **38** (1988) 1008.
- [10] D. A. Dicus, C. Kao and W. W. Repko, *Gluon Production of Gauge Bosons*, Phys. Rev. D **36** (1987) 1570.

- [11] E. W. N. Glover and J. J. van der Bij, *Z BOSON PAIR PRODUCTION VIA GLUON FUSION*, *Nucl. Phys. B* **321** (1989) 561.
- [12] A. Hasselhuhn, T. Luthe and M. Steinhauser, *On top quark mass effects to $gg \rightarrow ZH$ at NLO*, *JHEP* **01** (2017) 073 [1611.05881].
- [13] J. Davies, G. Mishima and M. Steinhauser, *Virtual corrections to $gg \rightarrow ZH$ in the high-energy and large- m_t limits*, *JHEP* **03** (2021) 034 [2011.12314].
- [14] K. Melnikov and M. Dowling, *Production of two Z-bosons in gluon fusion in the heavy top quark approximation*, *Phys. Lett. B* **744** (2015) 43 [1503.01274].
- [15] J. M. Campbell, R. K. Ellis, M. Czakon and S. Kirchner, *Two loop correction to interference in $gg \rightarrow ZZ$* , *JHEP* **08** (2016) 011 [1605.01380].
- [16] J. Davies, G. Mishima, M. Steinhauser and D. Wellmann, *$gg \rightarrow ZZ$: analytic two-loop results for the low- and high-energy regions*, *JHEP* **04** (2020) 024 [2002.05558].
- [17] G. Wang, X. Xu, Y. Xu and L. L. Yang, *Next-to-leading order corrections for $gg \rightarrow ZH$ with top quark mass dependence*, *Phys. Lett. B* **829** (2022) 137087 [2107.08206].
- [18] L. Alasfar, G. Degrandi, P. P. Giardino, R. Gröber and M. Vitti, *Virtual corrections to $gg \rightarrow ZH$ via a transverse momentum expansion*, *JHEP* **05** (2021) 168 [2103.06225].
- [19] G. Degrandi, R. Gröber and M. Vitti, *Virtual QCD corrections to $gg \rightarrow ZZ$: top-quark loops from a transverse-momentum expansion*, *JHEP* **07** (2024) 244 [2404.15113].
- [20] L. Chen, G. Heinrich, S. P. Jones, M. Kerner, J. Klappert and J. Schlenk, *ZH production in gluon fusion: two-loop amplitudes with full top quark mass dependence*, *JHEP* **03** (2021) 125 [2011.12325].
- [21] B. Agarwal, S. P. Jones and A. von Manteuffel, *Two-loop helicity amplitudes for $gg \rightarrow ZZ$ with full top-quark mass effects*, *JHEP* **05** (2021) 256 [2011.15113].
- [22] L. Chen, J. Davies, G. Heinrich, S. P. Jones, M. Kerner, G. Mishima et al., *ZH production in gluon fusion at NLO in QCD*, *JHEP* **08** (2022) 056 [2204.05225].
- [23] B. Agarwal, S. Jones, M. Kerner and A. von Manteuffel, *Complete Next-to-Leading Order QCD Corrections to ZZ Production in Gluon Fusion*, *Phys. Rev. Lett.* **134** (2025) 031901 [2404.05684].
- [24] J. Davies, G. Mishima, K. Schönwald and M. Steinhauser, *Analytic approximations of $2 \rightarrow 2$ processes with massive internal particles*, *JHEP* **06** (2023) 063 [2302.01356].

- [25] A. von Manteuffel and L. Tancredi, *The two-loop helicity amplitudes for $gg \rightarrow V_1 V_2 \rightarrow 4$ leptons*, *JHEP* **06** (2015) 197 [1503.08835].
- [26] F. Caola, J. M. Henn, K. Melnikov, A. V. Smirnov and V. A. Smirnov, *Two-loop helicity amplitudes for the production of two off-shell electroweak bosons in gluon fusion*, *JHEP* **06** (2015) 129 [1503.08759].
- [27] L. Bellafronte, G. Degrossi, P. P. Giardino, R. Gröber and M. Vitti, *Gluon fusion production at NLO: merging the transverse momentum and the high-energy expansions*, *JHEP* **07** (2022) 069 [2202.12157].
- [28] G. Degrossi, R. Gröber, M. Vitti and X. Zhao, *On the NLO QCD corrections to gluon-initiated ZH production*, *JHEP* **08** (2022) 009 [2205.02769].
- [29] F. Maltoni, M. K. Mandal and X. Zhao, *Top-quark effects in diphoton production through gluon fusion at next-to-leading order in QCD*, *Phys. Rev. D* **100** (2019) 071501 [1812.08703].
- [30] L. Chen, G. Heinrich, S. Jahn, S. P. Jones, M. Kerner, J. Schlenk et al., *Photon pair production in gluon fusion: Top quark effects at NLO with threshold matching*, *JHEP* **04** (2020) 115 [1911.09314].
- [31] M. Becchetti, F. Coro, C. Nega, L. Tancredi and F. J. Wagner, *Analytic two-loop amplitudes for $q\bar{q} \rightarrow \gamma\gamma$ and $gg \rightarrow \gamma\gamma$ mediated by a heavy-quark loop*, *JHEP* **06** (2025) 033 [2502.00118].
- [32] T. Ahmed, A. Chakraborty, E. Chaubey and M. Kaur, *Two-loop helicity amplitudes for diphoton production with massive quark loop*, 2502.03282.
- [33] P. Nogueira, *Automatic Feynman Graph Generation*, *J. Comput. Phys.* **105** (1993) 279.
- [34] M. Gerlach, F. Herren and M. Lang, *tapir: A tool for topologies, amplitudes, partial fraction decomposition and input for reductions*, *Comput. Phys. Commun.* **282** (2023) 108544 [2201.05618].
- [35] R. Harlander, T. Seidensticker and M. Steinhauser, *Complete corrections of Order α_s to the decay of the Z boson into bottom quarks*, *Phys. Lett. B* **426** (1998) 125 [hep-ph/9712228].
- [36] T. Seidensticker, *Automatic application of successive asymptotic expansions of Feynman diagrams*, in *6th International Workshop on New Computing Techniques in Physics Research: Software Engineering, Artificial Intelligence Neural Nets, Genetic Algorithms, Symbolic Algebra, Automatic Calculation*, 5, 1999, hep-ph/9905298.
- [37] B. Ruijl, T. Ueda and J. Vermaseren, *FORM version 4.2*, 1707.06453.

- [38] J. Davies, G. Heinrich, S. P. Jones, M. Kerner, G. Mishima, M. Steinhauser et al., *Double Higgs boson production at NLO: combining the exact numerical result and high-energy expansion*, *JHEP* **11** (2019) 024 [1907.06408].
- [39] J. Davies, G. Mishima, M. Steinhauser and D. Wellmann, *Double-Higgs boson production in the high-energy limit: planar master integrals*, *JHEP* **03** (2018) 048 [1801.09696].
- [40] J. Davies, G. Mishima, M. Steinhauser and D. Wellmann, *Double Higgs boson production at NLO in the high-energy limit: complete analytic results*, *JHEP* **01** (2019) 176 [1811.05489].
- [41] J. Klappert, F. Lange, P. Maierhöfer and J. Usovitsch, *Integral reduction with Kira 2.0 and finite field methods*, *Comput. Phys. Commun.* **266** (2021) 108024 [2008.06494].
- [42] A. V. Smirnov and F. S. Chukharev, *FIRE6: Feynman Integral REduction with modular arithmetic*, *Comput. Phys. Commun.* **247** (2020) 106877 [1901.07808].
- [43] A. V. Smirnov and M. Zeng, *FIRE 6.5: Feynman integral reduction with new simplification library*, *Comput. Phys. Commun.* **302** (2024) 109261 [2311.02370].
- [44] R. Bonciani, G. Degrossi, P. P. Giardino and R. Gröber, *Analytical Method for Next-to-Leading-Order QCD Corrections to Double-Higgs Production*, *Phys. Rev. Lett.* **121** (2018) 162003 [1806.11564].
- [45] J. Goode, F. Herzog and S. Teale, *OPITeR: A program for tensor reduction of multi-loop Feynman integrals*, *Comput. Phys. Commun.* **312** (2025) 109606 [2411.02233].
- [46] R. N. Lee, *LiteRed 1.4: a powerful tool for reduction of multiloop integrals*, *J. Phys. Conf. Ser.* **523** (2014) 012059 [1310.1145].
- [47] M. Fael, F. Lange, K. Schönwald and M. Steinhauser, *A semi-analytic method to compute Feynman integrals applied to four-loop corrections to the $\overline{\text{MS}}$ -pole quark mass relation*, *JHEP* **09** (2021) 152 [2106.05296].
- [48] M. Fael, F. Lange, K. Schönwald and M. Steinhauser, *A semi-numerical method for one-scale problems applied to the $\overline{\text{MS}}$ -on-shell relation*, *SciPost Phys. Proc.* **7** (2022) 041 [2110.03699].
- [49] M. Fael, F. Lange, K. Schönwald and M. Steinhauser, *Singlet and nonsinglet three-loop massive form factors*, *Phys. Rev. D* **106** (2022) 034029 [2207.00027].
- [50] G. Mishima, *High-Energy Expansion of Two-Loop Massive Four-Point Diagrams*, *JHEP* **02** (2019) 080 [1812.04373].

- [51] S. A. Larin, *The Renormalization of the axial anomaly in dimensional regularization*, *Phys. Lett. B* **303** (1993) 113 [[hep-ph/9302240](#)].
- [52] S. Catani, *The Singular behavior of QCD amplitudes at two loop order*, *Phys. Lett. B* **427** (1998) 161 [[hep-ph/9802439](#)].
- [53] Ancillary files at: <https://www.ttp.kit.edu/preprints/2025/ttp25-029/>.
- [54] A. van Hameren, *OneLOop: For the evaluation of one-loop scalar functions*, *Comput. Phys. Commun.* **182** (2011) 2427 [[1007.4716](#)].
- [55] G. Heinrich, S. P. Jones, M. Kerner, G. Luisoni and E. Vryonidou, *NLO predictions for Higgs boson pair production with full top quark mass dependence matched to parton showers*, *JHEP* **08** (2017) 088 [[1703.09252](#)].
- [56] S. Borowka, G. Heinrich, S. Jahn, S. P. Jones, M. Kerner, J. Schlenk et al., *pySecDec: a toolbox for the numerical evaluation of multi-scale integrals*, *Comput. Phys. Commun.* **222** (2018) 313 [[1703.09692](#)].
- [57] S. Borowka, G. Heinrich, S. Jahn, S. P. Jones, M. Kerner and J. Schlenk, *A GPU compatible quasi-Monte Carlo integrator interfaced to pySecDec*, *Comput. Phys. Commun.* **240** (2019) 120 [[1811.11720](#)].
- [58] G. Heinrich, S. Jahn, S. P. Jones, M. Kerner, F. Langer, V. Magerya et al., *Expansion by regions with pySecDec*, *Comput. Phys. Commun.* **273** (2022) 108267 [[2108.10807](#)].
- [59] M. Becchetti, R. Bonciani, L. Cieri, F. Coro and F. Ripani, *Two-loop form factors for diphoton production in quark annihilation channel with heavy quark mass dependence*, *JHEP* **12** (2023) 105 [[2308.11412](#)].
- [60] M. Becchetti, R. Bonciani, L. Cieri, F. Coro and F. Ripani, *Full top-quark mass dependence in diphoton production at NNLO in QCD*, *Phys. Lett. B* **848** (2024) 138362 [[2308.10885](#)].
- [61] T. Gehrmann, L. Tancredi and E. Weihs, *Two-loop QCD helicity amplitudes for $g g \rightarrow Z g$ and $g g \rightarrow Z \gamma$* , *JHEP* **04** (2013) 101 [[1302.2630](#)].
- [62] M. Grazzini, S. Kallweit and D. Rathlev, *$W\gamma$ and $Z\gamma$ production at the LHC in NNLO QCD*, *JHEP* **07** (2015) 085 [[1504.01330](#)].
- [63] F. Buccioni, F. Devoto, A. Djouadi, J. Ellis, J. Quevillon and L. Tancredi, *Interference effects in $g g \rightarrow H Z \gamma$ beyond leading order*, *Phys. Lett. B* **851** (2024) 138596 [[2312.12384](#)].
- [64] D. Lombardi, M. Wiesemann and G. Zanderighi, *Advancing M_{NNLO}_{PS} to diboson processes: $Z\gamma$ production at NNLO+PS*, *JHEP* **06** (2021) 095 [[2010.10478](#)].

- [65] M. Wieseemann, L. Rottoli and P. Torrielli, *The $Z\gamma$ transverse-momentum spectrum at NNLO+N³LL*, *Phys. Lett. B* **809** (2020) 135718 [2006.09338].
- [66] T. Hahn and M. Perez-Victoria, *Automatized one loop calculations in four-dimensions and D-dimensions*, *Comput. Phys. Commun.* **118** (1999) 153 [hep-ph/9807565].
- [67] B. Campillo Aveleira et al., *$gg \rightarrow ZH$: updated predictions at NLO QCD*, 8, 2025, 2508.09905.
- [68] J. Davies, K. Schönwald, M. Steinhauser and D. Stremmer, *ggxy: a flexible library to compute gluon-induced cross sections*, 2506.04323.